

Highlights

The influence of constraint on fracture toughness: Comparing theoretical T_0 shifts in master curve analyses with experimental data

A.N. O'Connor, C.M. Davies, S.J. Garwood

- In-plane and out-of-plane constraint affects the toughness of low strength steel in both the fully ductile and ductile-to-brittle transition regions in different ways. Regardless of failure mode (i.e ductile or brittle fracture), high in-plane constraint ($a/W = 0.5$) tests show more effect of out-of-plane constraint (thickness) compared to lower in-plane constraint tests ($a/W = 0.2$).
- Deeply notched ($a/W = 0.5$) bend tests show a clear dependency on out-of-plane (thickness) constraint condition for cleavage fracture. This finding is in agreement with thickness characteristics covered by design curves in the low temperature annexes of the Pressure Vessel codes BSI PD 5500 and EN 13445. The results of this test programme can be used to assess the conservatism of these codes for low strength steels used for as-welded applications at low temperatures.
- Shallow notched ($a/W = 0.2$) bend tests do not indicate the same thickness dependency seen in deeply notched ($a/W \geq 0.5$) tests for cleavage failure at various temperatures and geometries. Hence the use of results from shallow notch geometries for the assessment of the low temperature pressurised components must be handled with caution.

The influence of constraint on fracture toughness: Comparing theoretical T_0 shifts in master curve analyses with experimental data

A.N. O'Connor^{a,b}, C.M. Davies^a, S.J. Garwood^a

^a*Imperial College London, South Kensington, London, SW7 2BX, UK*

^b*University of Limerick, Limerick, V94 T9PX, Ireland*

Abstract

Quantifying the relationship between crack tip constraint and fracture toughness is key to improving the structural integrity assessment of critical infrastructure. The role of in-plane and out-of-plane constraint on fracture toughness requires greater understanding, particularly for low strength materials where test data are limited. In this work a structural steel, grade S275, is assessed both experimentally and via computational methods to investigate the role of constraint on fracture toughness. Single edge notch bend (SENB) samples, tested under three point bend conditions, at temperatures within the ductile-to-brittle transition range (+20 °C to −70 °C) are presented. Both standard ($B = W$, $B = 0.5W$) and non-standard ($B = 0.75W$, $B = 0.25W$) bend test geometries are assessed. Here it is shown that the in-plane and out-of-plane constraint parameters are interdependent. Out-of-plane (thickness) constraint trends which are generally accepted to occur under high in-plane conditions are not present when the in-plane constraint is reduced. The amount of ductile tearing incurred during fracture toughness

Email address: `alison.oconnor@ul.ie` (A.N. O'Connor)

testing is typically greater when both in-plane and out-of-plane constraint is reduced. Additionally thin samples are shown to be more ductile compared to thicker samples for samples with equivalent in-plane conditions. These findings have particular relevance to pressurised components operating at low temperatures.

Keywords:

fracture mechanics; master curve; constraint; fracture toughness;

1. Introduction

Protecting components such as pressure vessels from brittle fracture is of paramount importance. The origins and development of the British and European code rules governing the operation of pressure vessels at low temperatures are outlined in more detail elsewhere [1, 2, 3, 4] but a brief review is provided in the following paragraphs.

The British code, PD 5500 [5], developed a relationship between design reference temperature and Charpy impact test temperature for a range of plate thicknesses. These ‘design curves’ were based on a mixture of practical experience supported by experimental validation. The validation work included the comparison of 1 m², through notched, wide plate specimens with standard fracture toughness single edge notch bend (SENB) specimens. The results of these tests were linked to the temperatures at which Charpy energies of 27 J or 41 J (dependent on the material yield strength) are achieved [6, 7]. In essence, although not explicitly, the design curves allowed for in-plane and out-of-plane constraint effects through calibration with Charpy and SENB specimen types i.e. in-plane constraint effects being assessed through

the use of deeply notched ($a/W = 0.5$) SENB specimens while out-of-plane constraint effects were assessed through the use of full thickness SENB and plate specimens.

The European code, EN 13445, historically developed as “a combination of relevant existing national codes” [6] resulting in design curves that were similar to those in PD 5500 for comparable plate thicknesses [2]. In recent years newer revisions of EN 13445 [8] have adopted an analytical approach to deriving the design curve relationship. This resulted in significant changes to the design curve relationship, with less onerous Charpy test temperatures being required, compared with PD 5500, for lower design reference temperatures. Experimental validation for these new design curves was however limited to high strength materials resulting in some ambiguity as to their relevance to lower strength materials, particularly for components without post-weld heat treatment.

Since the original development of these standards, significant research has been carried out on the use of a master curve approach [9] based on the fracture toughness of 25 mm thick compact tension specimens. The master curve method statistically describes the relationship between fracture toughness and test temperature and allows for variations of out-of-plane constraint (sometimes termed “the thickness effect”) through normalising thicknesses to a nominal 1 inch thickness. Later modifications [10] used a two-parameter fracture approach to assess how in-plane constraint resulted in changes to the master curve. The master curve approach uses a reference temperature, T_0 , to relate toughness and temperature. The reference temperature itself is determined directly from fracture toughness data and is simply the temper-

ature at which toughness is $100 \text{ MPa}\sqrt{m}$.

Many experimental studies of constraint effects on both ductile and brittle behaviour have been conducted, but the results have been dominated by material scatter and/or complex loading configurations [11, 12, 13, 14, 15, 16, 17, 18, 19, 20]. Furthermore, the effect of constraint on fracture toughness varies depending on whether brittle fracture occurs under small-scale or large-scale yielding behaviour. The test programme described in this paper is part of a study designed to assess the validity of the design curves in the most recent revision of EN 13445 for lower strength materials. Here tests were performed on a low strength ferritic material ($\sigma_y \geq 275 \text{ MPa}$ at room temperature) over a range of test temperatures and with varying levels of crack tip constraint. Deeply notched SENB specimens ($a/W = 0.5$) were used to assess how out-of-plane (thickness) effects contribute to fracture toughness and in turn provide some confidence in whether the pressure vessel design codes characterise out-of-plane (thickness effects) appropriately. Shallow notched SENB specimens ($a/W = 0.2$) were also investigated to assess whether the thickness effects evident in deeply notched specimens are comparable when the in-plane constraint parameter is significantly reduced.

2. Experimental test methods

A 40 mm thick plate of plain material, grade S275, was used in this work. Specimens were extracted from the plate in accordance with BS EN ISO 3785 [21], see Figure 1. To ensure material homogeneity, specimens were manufactured from the mid-thickness of the plate (i.e. mid-thickness of the Z-axis).

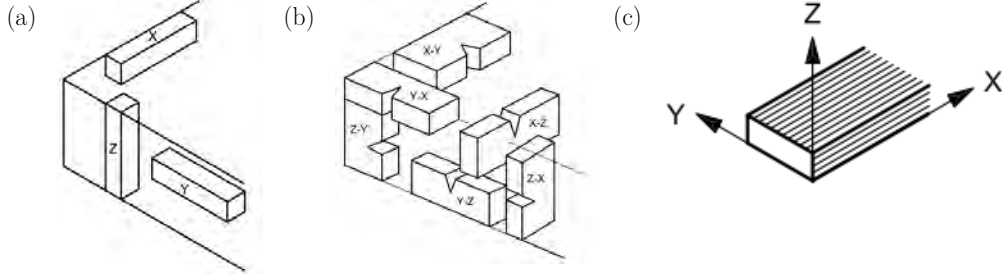


Figure 1: Specimen axes oriented with respect to grain flow as per [21]. (a) unnotched geometries, (b) notched geometries and (c) grain flow orientation.

Testing was conducted at temperatures in the range of $+100\text{ }^{\circ}\text{C}$ to $-70\text{ }^{\circ}\text{C}$. Room temperature tests ($+20\text{ }^{\circ}\text{C}$) were conducted in air. Low temperature test specimens ($\leq 20\text{ }^{\circ}\text{C}$) were placed into an Instron 3119-005 environmental chamber and cooled to the required test temperature using liquid nitrogen. The temperature was controlled electronically to within $\pm 0.5\text{ }^{\circ}\text{C}$ for the duration of testing.

2.1. Charpy impact toughness

A total of 63 Charpy impact toughness specimens ($10 \times 10 \times 55\text{ mm}$) were manufactured. Approximately 30 specimens were oriented and notched in X-Y plane, the remaining specimens were oriented in the Y-X plane (Figure 1b). Testing was conducted in a ZwickRoell pendulum impact testing machine.

To define the upper and lower shelf and the ductile-to-brittle transition region of the material testing was conducted in the temperature range $+100\text{ }^{\circ}\text{C}$ to $-60\text{ }^{\circ}\text{C}$ for Y-X specimens and, $+100\text{ }^{\circ}\text{C}$ to $-70\text{ }^{\circ}\text{C}$ for X-Y specimens. To ensure a statistically relevant average of impact energy could be assessed a minimum of 3 specimens were tested per temperature per orientation.

Wallin [9] showed that, for ferritic steels, the shape of the relationship be-

tween temperature and toughness is fixed. The master curve for specific materials can therefore be described via a reference temperature. The reference temperature (T_0) is often used to define the onset of lower shelf cleavage behaviour [22]. In the master curve the T_0 position is the temperature at which toughness is $100 \text{ MPa}\sqrt{m}$. An initial estimate of appropriate test temperatures for T_0 estimation can be made from Charpy impact testing data using Equations 1 and 2 [23]. The test method for determining T_0 [23] provides details on the value of the constant C for various specimen thicknesses. In this work all specimens are normalised to a 1 inch (25.4 mm) thickness. At a thickness of 1 inch the constant C has a temperature value of -18°C (T_{28J}) or -24°C (T_{41J}) temperatures, respectively. Once adjusted an estimated value of T_0 can be calculated using Equation 3. Later (Section 3.3.4), T_0 will be calculated from fracture toughness tests.

$$T_{CVN_{28J}} = T_{28J} + C \quad (1)$$

$$T_{CVN_{41J}} = T_{41J} + C \quad (2)$$

$$T_{0_{est}} = \frac{T_{CVN_{28J}} + T_{CVN_{41J}}}{2} \quad (3)$$

2.2. Tensile testing

Sixteen 10 mm diameter round bar specimens were machined from the plate material. To assess the influence of microstructure on the mechanical properties, specimens were manufactured in both the X and Y planes (Figure 1b). Testing was conducted in an Instron 5584 150 kN servo-electric test machine with an Instron environmental chamber. Strain was measured using

an Epsilon Model 3542 axial extensometer with a gauge length of 50 mm. To avoid damage, the extensometer was removed mid-way through testing.

Tensile testing was conducted in accordance with BS EN 10002-1 [24] at a displacement rate of 1 mm/minute until failure, at four test temperatures: room temperature (≈ 20 °C), -20 °C, -40 °C and -70 °C. At each temperature up to four specimens were tested, two oriented in the X plane and two oriented in the Y plane. Specimens were allowed to thermally equilibrate in the test chamber for approximately 30 minutes prior to starting the test.

The true strain-strain relationship was derived from engineering stress-strain data up to maximum load (σ_{UTS}) using Equations 4, 5. Where σ_{true} represents true stress, σ_{eng} engineering stress, ϵ_{true} true strain and ϵ_{eng} engineering strain. True stress-strain data were fitted using Equation 6, where σ represents stress, ϵ_p is plastic strain, A is a strength coefficient and n the strain hardening exponent.

$$\epsilon_{true} = \ln(1 + \epsilon_{eng}) \quad (4)$$

$$\sigma_{true} = \sigma_{eng}(1 + \epsilon_{eng}) \quad (5)$$

$$\sigma = A\epsilon_p^n \quad (6)$$

The mechanical performance of this material at any given test temperature can be estimated from room temperature material properties [25] using Equations 7 and 8. Here the term “assessment temperature” is used to describe the test temperature for which material properties are unknown. In

Equations 7 and 8 $\sigma_{y_{AT}}$ is the yield strength at the assessment temperature, $\sigma_{y_{RT}}$ the yield strength at room temperature and T the temperature of interest. Similarly $\sigma_{UTS_{RT}}$ and $\sigma_{UTS_{AT}}$ refer to the room and assessment temperature for the ultimate tensile strength.

$$\sigma_{y_{AT}} = \sigma_{y_{RT}} + \frac{10^5}{(491 + 1.8T)} - 189 \quad (7)$$

$$\sigma_{UTS_{AT}} = \sigma_{UTS_{RT}} \left[0.7857 + 0.2423 \times \exp\left(\frac{-T}{170.646}\right) \right] \quad (8)$$

British Standards Institute [25] also provides a method of estimating the stress-strain response from these general material properties as shown in Equations 9 - 11, where σ is the applied stress, E Young's Modulus, σ_y yield strength, ϵ_y strain at σ_y , ϵ_u uniform elongation strain at ultimate tensile strength, and σ_u tensile strength. Equation 12 may be applied for materials exhibiting Lüder's plateau.

$$\epsilon = \frac{\sigma}{E} + \frac{A_r \sigma_y}{E} + \left(\frac{\sigma}{\sigma_y} \right)^n \quad (9)$$

$$A_r = \frac{E \epsilon_y}{\sigma_y} - 1 \quad (10)$$

$$n = \frac{\log_{10} [(E \epsilon_u / \sigma_u) - 1] - \log_{10} [(E \epsilon_y / \sigma_y) - 1]}{\log_{10} (\sigma_u / \sigma_y)} + 1 \quad (11)$$

$$\Delta \epsilon = 0.0375 (1 - 0.001 \sigma_y) \quad (12)$$

2.3. Fracture toughness testing and estimation of T_0

Fracture toughness testing was conducted on single edge notch bend (SENB) specimens in accordance with ASTM E1820-20 test method [26]. Standard SENB specimens relate the specimen height (W) to the specimen thickness (B) and are generally either $B \times B$ or $B \times 2B$ in geometry. The specified [26] flaw depth (a) to specimen height (W) ratio of $a/W \geq 0.5$ promotes high in-plane constraint. The out-of-plane constraint is controlled by the specimen height to thickness ratio (W/B).

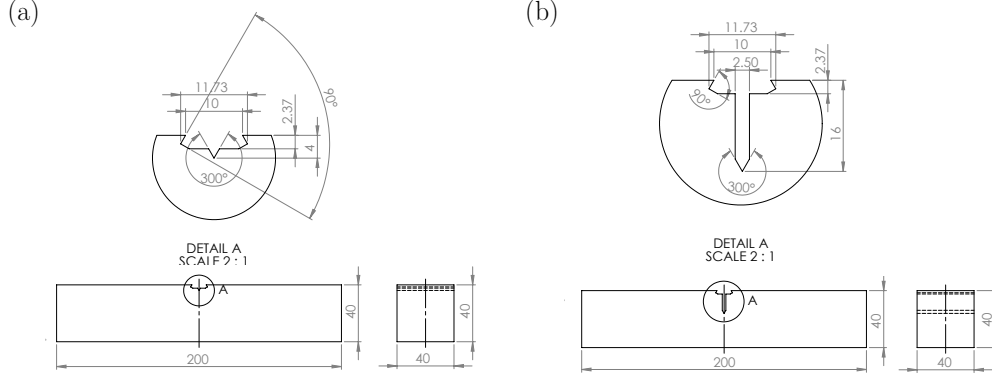


Figure 2: SENB specimen geometries showing machined (a) shallow notch geometry and (b) deeply notched geometry for $B \times B$ thickness.

In this work both the in-plane and out-of-plane constraint parameters were varied. Low in-plane constraint conditions were assessed using specimens with crack depth to specimen height ratios of $a/W = 0.2$ (Figure 2a). High in-plane constraint conditions $a/W = 0.5$ were also investigated [26] (Figure 2b). All specimens were fatigue pre-cracked from their machined condition (Figure 2) to the relevant initial fracture toughness test a/W ratio. Out-of-plane constraint was modified by fixing the specimen height ($W = 40$)

while varying specimen thickness (B). All SENB specimens were machined and notched in the X-Y plane (Figure 1b).

Crack mouth opening displacement (CMOD) was measured using an Instron 10 mm clip gauge located on the surface of the specimen in machine integrated knife edges. Fatigue pre-cracking was conducted in accordance with ISO 12135 [27], at room temperature, using a 200 kN hydraulic Instron test machine. As per requirements [27], the final 1.3 mm of fatigue pre-cracking load was achieved by reducing the applied load range. Pre-cracking specimens using this load-shedding method ensured the fatigue pre-crack remained relatively flat along the crack front.

Room temperature fracture toughness testing was conducted using a hydraulic 200 kN Instron test machine. Low temperature fracture toughness testing was conducted using a 150 kN servo-electric Instron test machine with an environmental chamber. Where relevant, specimens were allowed to thermally equilibrate to the required test temperature prior to testing by placing specimens into the cooled environmental chamber for a minimum of 30 min per 25 mm of specimen thickness [26]. Toughness testing followed the ASTM E1820 [26] basic test method and test specimens were loaded in three-point bending (3PB) until failure. Specimens were assumed to have failed if either the clip gauge reached maximum travel or a significant reduction in load occurred. The crosshead displacement, applied load and CMOD were measured continuously throughout testing.

The stress intensity factor was calculated from test data using Equation 13 where P_i represents applied load, S the span of the specimen, B specimen thickness, W specimen width, and a_i initial crack depth. The

toughness parameter ‘J’ was calculated from the elastic (Equation 15) and plastic contributions (Equation 16) as detailed in Equation 14. The plastic contribution J_{pl} is detailed in Equation 16 where the plastic area A_{pl} was calculated from test data, η_{pl} was assumed to have a value of 1.9, and b_0 represents the remaining ligament (i.e. $b_0 = W - a_i$). Using Equation 17, J values were corrected for crack growth, where α was assumed to be unity. ν represents Poisson’s ratio and was assumed to be 0.3 for this material.

$$K_i = \left[\frac{P_i S}{\sqrt{B^2} \sqrt[3]{W}} \right] f \left(\frac{a_i}{W} \right) \quad (13)$$

$$J = J_{el} + J_{pl(corr)} \quad (14)$$

$$J_{el} = \frac{K^2 (1 - \nu^2)}{E} \quad (15)$$

$$J_{pl} = \frac{\eta_{pl} A_{pl}}{B b_0} \quad (16)$$

$$J_{(corr)} = J_{el} + \frac{J_{pl}}{1 + \left(\frac{\alpha - 0.5}{\alpha + 0.5} \right) \frac{\Delta a}{b_0}} \quad (17)$$

To measure any crack extension occurred during fracture testing, in specimens which did not fail completely, post-test specimens were placed in a oven at 300° C for a minimum of two hours to heat-tint the fracture surface. After heat-tinting, specimens were allowed to cool to room temperature. Cooled specimens were then placed in a low temperature environment and loaded until cleavage fracture occurred. The fracture surface of each specimen was visually assessed. The amount, if any, of ductile tearing was measured at

a minimum of ten locations along the crack front of each specimen and the average crack depth through the thickness was calculated.

To investigate the reference temperature, T_0 , the standard test method E1921 [23] was employed. Stress intensity at the onset of cleavage fracture was estimated using Equation 18 where J^* represents J at the onset of cleavage fracture. To compare specimens across the range of thicknesses investigated, Equation 19 was used to normalise the thickness to a standard 1 inch (25.4 mm) thick specimen.

$$K_{Jc} = \sqrt{J^* \frac{E}{1 - \nu^2}} \quad (18)$$

$$K_{Jc_{1t}} = 20 + [K_{Jc} - 20] \left(\frac{B}{25.4} \right)^{1/4} \quad (19)$$

The Weibull fitting parameter, K_0 , was estimated as shown in Equation 20, where N represents the sample size, $K_{Jc(i)}$ the individual toughness value and r the number of uncensored data points. K_0 represents the 63.2% cumulative failure probability level. The median toughness is estimated from Equation 21 while T_0 is estimated via Equation 22. The standard deviation associated with the Weibull distribution was estimated as shown in Equation 23. Confidence intervals can be established through Equation 24 where C represents the 5% and 95% confidence in T_0 .

$$K_0 = \left[\sum_{i=1}^N \frac{\left(K_{Jc(i)} - 20 \right)^4}{r} \right] + 20 \quad (20)$$

$$K_{Jc_{med}} = 20 + 0.91 (K_0 - 20) \quad (21)$$

$$T_0 = T - \left(\frac{1}{0.019} \right) \ln \left(\frac{(K_{Jc_{med}} - 30)}{70} \right) \quad (22)$$

$$\sigma = 0.28 K_{Jc_{med}} \left[1 - \frac{20}{K_{Jc_{med}}} \right] \quad (23)$$

$$K = 20 + \left[\ln \left(\frac{1}{1 - C} \right) \right]^{\frac{1}{4}} \times (11 + 77e^{0.019(T - T_0)}) \quad (24)$$

2.4. Finite element modelling (FEM)

Two-dimensional (2D) and three-dimensional (3D) finite element modelling (FEM) was conducted to investigate the theoretical response of samples under three point bend loading. The finite element model geometry was based on experimental specimen geometries with both $a/W = 0.2$ and $a/W = 0.5$ ratios for each specimen thickness $B = 10, 20, 30, 40$ mm. The pins used to support and load the specimen were modelled as analytical rigid shells. A frictionless, hard contact was specified between the surface of the specimen and the surface of the pins.

The crack tip was idealised as a sharp defect. Collapsed quadrilateral elements (wedge shaped) with duplicated nodes and a midside position of 0.25 were employed at the crack tip. Structured elements were used in all other locations. Room temperature material properties derived from mechanical testing (Table 4) were applied. Analyses were conducted using Abaqus 2018 [28].

The stress intensity factor (SIF), T-stress and toughness (J_k) were estimated over 20 contours. The two contours adjacent to the crack tip were discounted to avoid numerical inconsistencies. The remaining 18 contours

were averaged. Stress intensity factor (SIF), T-stress and toughness (J_k) values reported here are based on the average of the 18 contours as specified for each increment of loading.

2.4.1. Two-dimensional (2D) analyses

Linear-elastic models were used to compute T-stress for both plane strain and plane stress conditions. Non-linearity was assumed to be negligible (NLGEOM=OFF). The supporting rollers were constrained in all directions ($U1=U2=U3=0$), while the loading pin was constrained so as to displace in a linear fashion only ($U1=1$, $U2=U3=0$). Boundary conditions were applied to reference nodes in the centre of each pin and then coupled to the pin surface. A node on the specimen geometry, in contact with the loading pin, was constrained to prevent rigid body motion of the specimen ($U2=U3=0$). Element types CPE8R and CPS8R were applied to all regions for the plane strain and plane stress conditions, respectively. A minimum of 2500 elements, biased towards the crack tip region were employed as shown in Figure 3.

To assess the plastic collapse load under three-point bending, two dimensional (2D) elastic-plastic FEM analyses were also conducted. To account for large deformation at the crack tip region non-linearity was assessed (NLGEOM=ON). A plane strain condition was assumed. The boundary conditions and element selection were identical to those applied to the 2D linear-elastic plane strain simulations described above. Material properties were derived from experimental data assuming a power-law relationship (Equation 6).

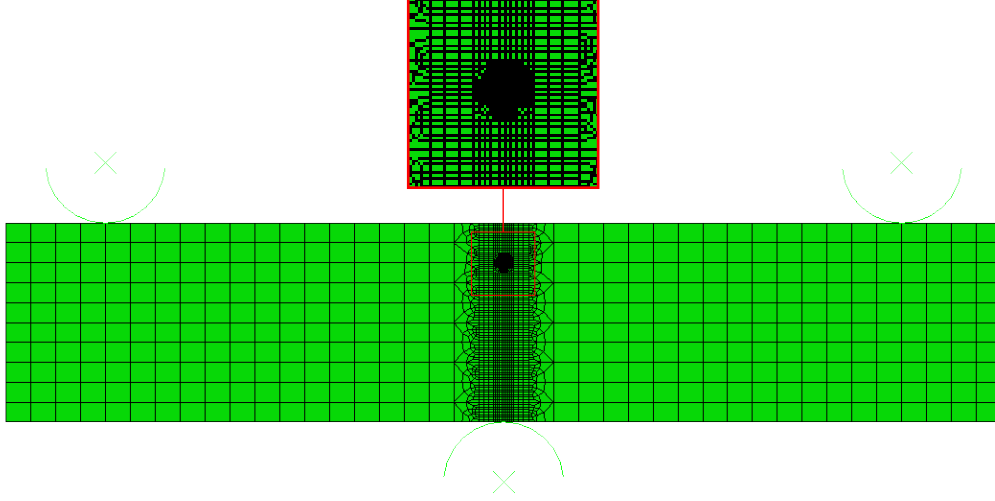


Figure 3: Mesh strategy used in 2D FEA analysis. The magnified region shows the mesh density surrounding the crack tip.

2.4.2. Three-dimensional (3D) analyses

Three-dimensional linear-elastic FEM was conducted to assess the influence of out-of-plane constraint on T-stress compared with 2D simulations. Non-linearity was assumed to be negligible (NLGEOM=OFF). The supporting rollers were constrained in all directions ($U1=U2=U3=0$ and $UR1=UR2=UR3=0$), while the loading pin was constrained so as to displace in a linear fashion only ($U1=1$, $U2=U3=UR1=UR2=UR3=0$). The boundary conditions were applied to reference nodes in the centre of each pin coupled to the pin surface. A node on the specimen geometry, in contact with the loading pin, was constrained to prevent rigid body motion of the specimen ($U2=U3=UR1=0$). Element type C3D20R were applied to all regions. The mesh strategy on the cracked plane is similar to that applied to the 2D case (Figure 3). In the thickness direction one element per 0.5

millimetre was applied as shown in Figure 4. Key fracture mechanics parameters: Stress intensity factor (SIF), T-stress and J values were estimated in the manner described previously at 0.5 mm intervals through the thickness.

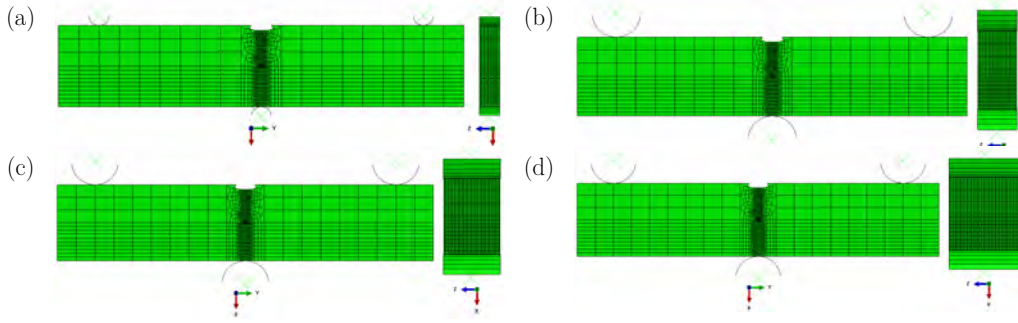


Figure 4: Mesh strategy used in 3D FEA analysis. Magnified region depicting mesh density surrounding crack tip.

3. Results

3.1. Charpy impact toughness

The minimum and standard deviation of Charpy energy for each specimen orientation and test temperature are shown in Figure 5. The upper shelf region was fitted assuming a linear relationship between energy and temperature, coefficients are provided in Table 1. The transition region was fitted assuming a two degree polynomial relationship, coefficients are provided in Table 2. All fitted data are based on minimum energy values over the appropriate temperature range depicted in Figure 5.

Comparing Figures 5a to 5b shows that the notch orientation influences the relationship between impact energy and temperature. This was not unexpected as the material was in an as-rolled condition. The measured T_{27J}

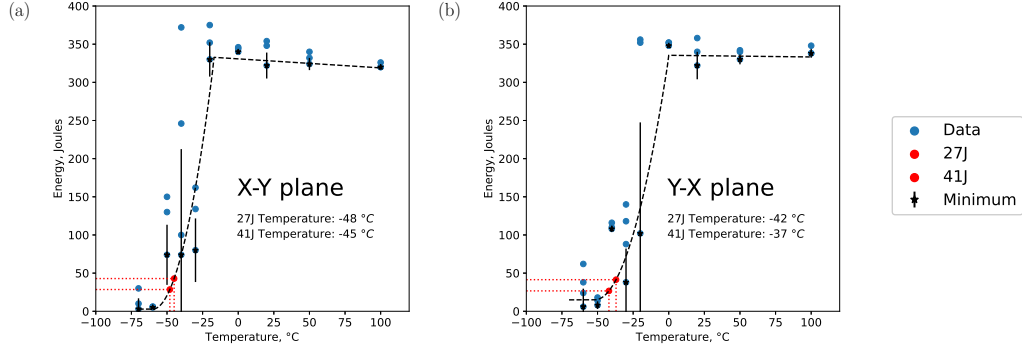


Figure 5: Impact energy versus temperature for (a) specimens notched in the X-Y plane and (b) specimens notched in the Y-X plane. Data fitted using the minimum energy value for each temperature.

Table 1: Coefficients for linear fit ($y = mx + c$) to upper shelf Charpy energy data

Coefficient	X-Y	Y-X
c	330.75	335.44
m	-0.12	-0.02
R^2	0.47	0.01

Table 2: Coefficients for two degree polynomial fit ($y = Ax^2 + Bx + C$) to transition region Charpy energy data

Coefficient	X-Y	Y-X
A	0.18	0.12
B	21.19	12.23
C	639.29	332.95

and T_{41J} temperatures were adjusted, as outlined in the methods section, and an initial estimate of T_0 calculated (Equation 3). Table 3 shows that the T_0 estimated from Charpy energy is in the range $-67.5 \geq T_0 \geq -60.5$ °C.

Table 3: Initial estimate of T_0 using temperatures derived from best fit minimum Charpy impact energy values for two specimen orientations.

		Property	X-Y Plane	Y-X Plane
			°C	
From Figure 5	T_{27J}		-48	-42
	T_{41J}		-45	-37
From Equations 1 and 2	$T_{CVN_{28J}}$		-66	-60
	$T_{CVN_{41J}}$		-69	-61
From Equation 3	$T_{0_{est}}$		-67.5	-60.5

3.2. Mechanical properties

To assess whether specimen orientation (X plane or Y plane) influenced the mechanical properties, specimens were compared, at each test temperature, for both orientations. The mechanical response was noted to be independent of specimen orientation thus, for each test temperature, data for: load, extension, and stress, were averaged for comparable measures of strain. The averaged data was smoothed using a moving average with a window of 20 strain measurements. The smoothed data representing the average ‘engineering’ mechanical response at each test temperature are shown in Figure 6.

Engineering stress-strain data were converted to true stress-true strain using Equations 4 and 5 up to maximum load (σ_{UTS}). Table 4 details

the key mechanical properties. The plastic region of the true stress-strain curve was fit using the power law relationship in Equation 6. Parameters A and n in Table 4 represents the best fit between a power law relationship (Equation 6) and test data up to maximum load. Results are as expected with yield strength increasing as test temperature decreases. As the extensometer was removed mid-way through testing the failure strain in Table 4, $\epsilon_{failure}$, was estimated using the crosshead displacement at fracture and the specimen gauge length.

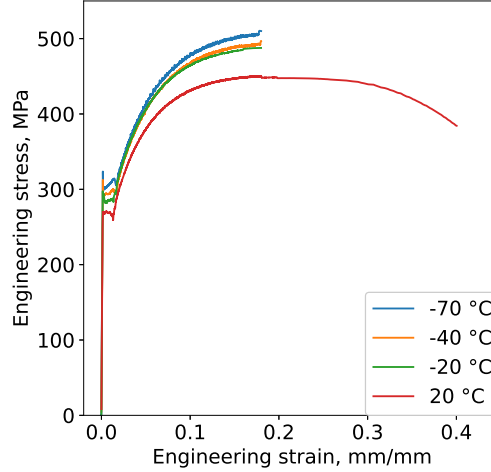


Figure 6: Averaged engineering stress-strain relationship for each test temperature

3.2.1. Comparison with BS 7910 methods

In many cases, structural integrity assessments are conducted on existing structures where mechanical testing is not possible. In these cases knowledge of the mechanical properties may be limited to data provided in the materials certification. The material certification of this material specified the mechanical properties at room temperature to be $\sigma_y = 293$ MPa and

Table 4: Average mechanical properties at each test temperature. Parameters A and n represent the best fit for a power law relationship (Equation 6 to test data up to maximum load (σ_{UTS})).

Mechanical Property	Units	Test temperature, °C			
		20	-20	-40	-70
Young’s modulus (E)	GPa	209.0	219.4	214.6	207.5
0.2% σ_y	MPa	267.3	287.4	292.2	300.4
σ_{UTS}	MPa	450.6	487.7	496.9	510.5
ϵ_{UTS}	-	0.18	0.18	0.18	0.18
$\epsilon_{failure}$	-	0.37	0.24	0.24	0.25
A	MPa	865.3	959.7	977.4	1007.4
n	-	0.26	0.27	0.28	0.28

$\sigma_{UTS} = 458$ MPa. These values were incorporated into Equations 7 and 8 to estimate mechanical properties at the relevant test temperature. The Young’s modulus were estimated by interpolation from Table 7.3 in BS 7910 [25]. The stress-strain relationship was developed from Equations 9-11. To account for the Lüder’s plateau the change in strain, occurring at the yield strength, was calculated using Equation 12. Strains estimated from Equations 9-11 were then increased by $\Delta\epsilon$ for stresses exceeding the assessment temperature yield strength.

Figure 7 compares the average mechanical response measured during testing with the estimated mechanical response derived using the BS 7910 method. At all temperatures the yield strength of the material is overestimated compared to those measured experimentally. At a test temperature of

$-70\text{ }^{\circ}\text{C}$ the prediction overestimated the yield strength by $\approx 80\text{ MPa}$ compared to the measured value. The implication here is that the application of Equation 7 may lead to somewhat unconservative estimates of yield strength, particularly at test temperatures lower than $-70\text{ }^{\circ}\text{C}$. The estimated UTS at each temperature is within $\pm 30\text{ MPa}$ of the measured UTS, this is considered good agreement. Generally the Lüder’s plateau was captured quite well the exception perhaps being the room temperature ($20\text{ }^{\circ}\text{C}$) condition where the BS 7910 method appears to have over estimated the extent of the plateau. The hardening ability of the material appears to be captured quite well using the standard but the elongation characteristics are generally better captured for test temperatures $> -40\text{ }^{\circ}\text{C}$.

The main function of deriving the stress-strain relationship for structural integrity assessments lies in the creation of a failure assessment diagram (FAD) [25]. A FAD is bounded by a curve which is essentially defined by the mechanical properties. Hence the mechanical properties of the material will significantly influence the structural integrity assessment result and therefore directly impact the estimated life-cycle of the component. The relatively good agreement found here between estimated and measured mechanical properties will result in FADs that are virtually identical regardless of whether estimated or measured properties are employed. As such the BS 7910 method for estimating mechanical properties is considered to be appropriate for low strength ferritic steels.

3.3. Fracture toughness

The single edge notch bend (SENB) specimens were identified by notch depth, specimen thickness, test temperature and specimen number. Hence

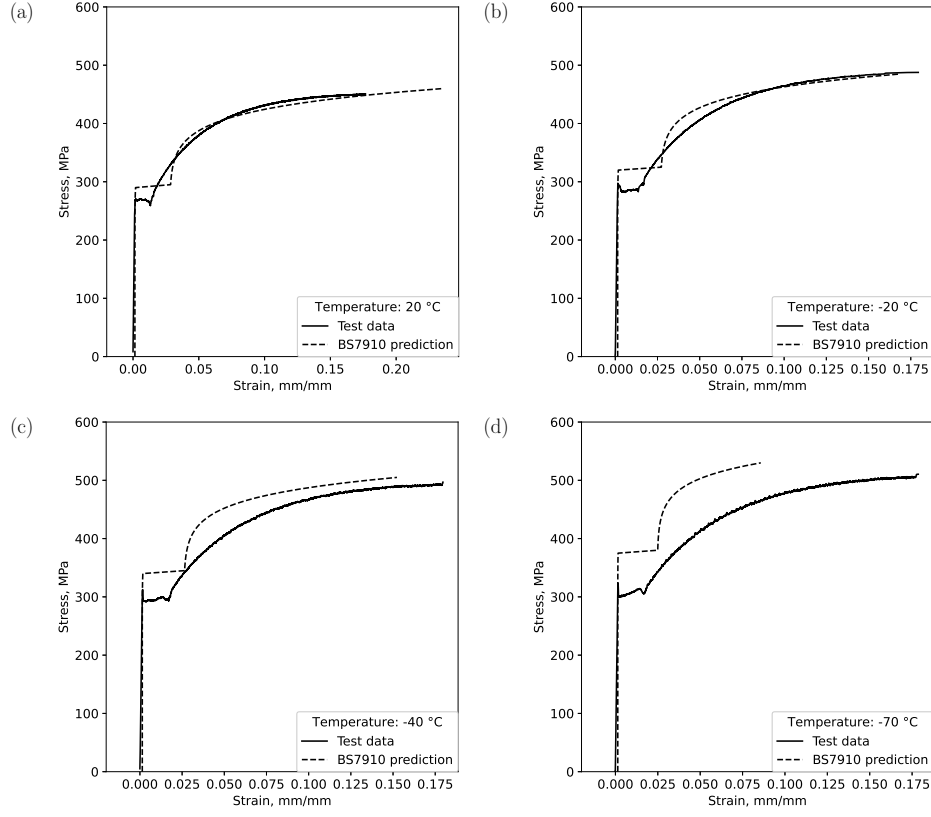


Figure 7: Comparison of mechanical properties derived from testing with estimated mechanical properties derived using BS 7910 method for test temperatures of (a) 20 °C, (b) -20 °C, (c) -40 °C, (d) -70 °C

a sample labelled 'D40RT2' is a deeply notched ($a/W = 0.5$) 40 mm thick specimen tested at room temperature and is the second such specimen tested. Similarly S20-401 is a shallow notched ($a/W = 0.2$) 20 mm thick specimen tested at -40 °C and is the first specimen tested. At temperatures > -40 °C all but one of the reported CMOD values represent interrupted tests where the maximum clip-gauge extension has been attained. The reported CMOD values for test temperatures of -40 °C and -70 °C represent failure of the

specimen.

3.3.1. Investigating force versus crack mouth opening an initial data assessment

The load versus crack mouth opening displacement (CMOD) are shown in Figure 8 for high in-plane constraint conditions ($a/W = 0.5$) and Figure 9 for low in-plane constraint conditions ($a/W = 0.2$), respectively. For comparison purposes plots are segregated by test temperature with (a) representing $+20\text{ }^{\circ}\text{C}$, (b) representing $-20\text{ }^{\circ}\text{C}$, (c) representing $-40\text{ }^{\circ}\text{C}$, and (d) representing $-70\text{ }^{\circ}\text{C}$. As multiple identical tests were conducted the final load versus CMOD positions are identified using symbols. Specimens ending in '1' with 'X' symbol, specimens ending in '2' with '+' symbol, specimen ending in '3' with '.' symbol. The final load and CMOD values (i.e. symbols in Figures 8 and Figure 9) are tabulated in Table 5 for a test temperature of $+20\text{ }^{\circ}\text{C}$ to Table 8 for a test temperature of $-70\text{ }^{\circ}\text{C}$, respectively.

Comparing the high in-plane constraint condition ($a/W = 0.5$) to low in-plane constraint condition ($a/W = 0.2$) at room temperature ($\approx 20\text{ }^{\circ}\text{C}$, Figures 8a and 9a and Table 5) it is shown that, regardless of in-plane constraint condition, the maximum CMOD of the gauge was achieved. This was as expected given that at $+20\text{ }^{\circ}\text{C}$ Figure 5 indicated upper shelf behaviour and thus all specimens were expected to fail by ductile tearing only. The greatest difference comparing the in-plane constraint conditions are seen in terms of applied load. This is in agreement with literature [1, 16, 17, 22, 29, 30]. Low in-plane constraint conditions ($a/W = 0.2$) reached far greater magnitudes of load compared to high in-plane constraint samples of similar thicknesses. This is not unexpected given the remaining ligament of low in-plane con-

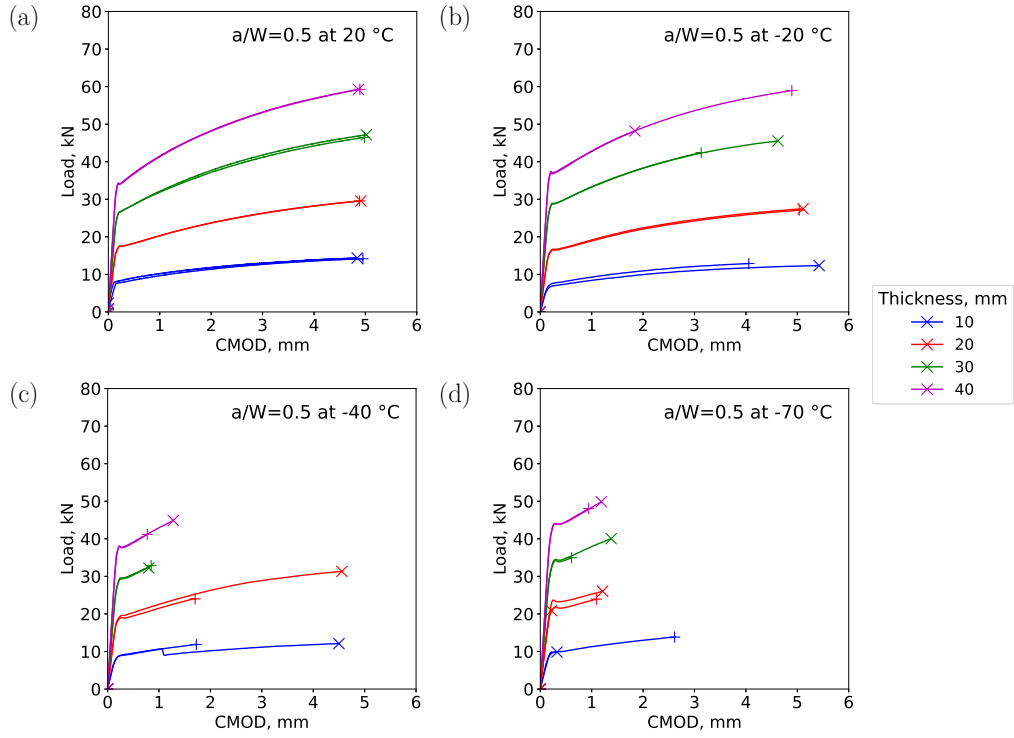


Figure 8: Force versus crack mouth opening displacement (CMOD) for high in-plane constraint condition ($a/W = 0.5$) at (a) 20°C, (b) -20°C, (c) -40°C, (d) -70°C test temperature. The final CMOD position is identified for geometrically identical specimens tested at the same temperature as follows: Specimens ending in '1' with 'X' symbol, specimens ending in '2' with '+' symbol, specimen ending in '3' with '.' symbol.

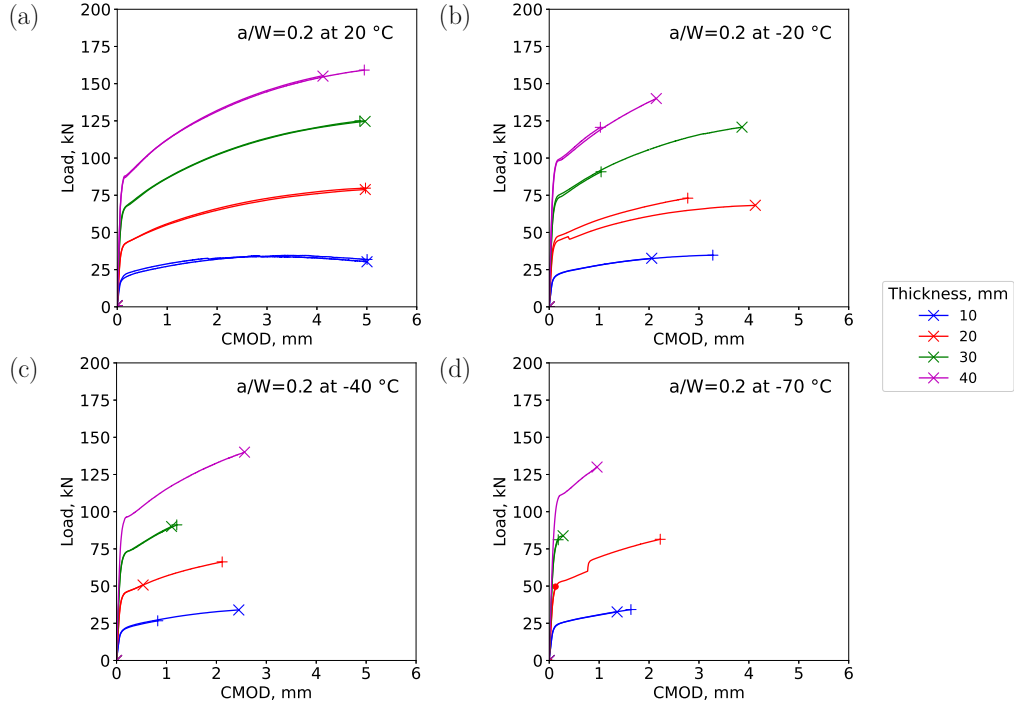


Figure 9: Force versus crack mouth opening displacement (CMOD) for low in-plane constraint condition ($a/W = 0.2$) at (a) 20°C (tests interrupted at max CMOD), (b) -20°C, (c) -40°C, (d) -70°C test temperature. The final CMOD position is identified for geometrically identical specimens tested at the same temperature as follows: Specimens ending in '1' with 'X' symbol, specimens ending in '2' with '+' symbol, specimen ending in '3' with '.' symbol.

Table 5: Final load and crack mouth opening displacement (CMOD) values for test temperature of 20 °C

Thickness mm	a/W -	Specimen Name -	CMOD mm	Load kN
10.0	0.2	S10RT1	5.00*	30.32
	0.2	S10RT2	5.00*	31.86
	0.5	D10RT1	4.84	14.34
	0.5	D10RT2	4.95	14.15
20.0	0.2	S20RT1	4.97	78.83
	0.2	S20RT2	4.97	79.80
	0.5	D20RT1 ⁺	4.91	29.56
	0.5	D20RT2	4.89	29.56
30.0	0.2	S30RT1	4.97	124.64
	0.2	S30RT2	4.86	124.95
	0.5	D30RT1	5.02*	47.17
	0.5	D30RT2	4.98	46.48
40.0	0.2	S40RT1	4.12	155.06
	0.2	S40RT2	4.95	159.16
	0.5	D40RT1	4.87	59.23
	0.5	D40RT2	4.89	59.26

* Maximum CMOD measurable by clip gauge \approx 5.0 mm

⁺ Fracture surface image shown in Figure 10a

Table 6: Final load and crack mouth opening displacement (CMOD) values for test temperature of -20 °C

Thickness mm	a/W -	Specimen Name -	CMOD mm	Load kN
10.0	0.2	S10-201	2.05	32.60
	0.2	S10-202	3.28	34.73
	0.5	D10-201	5.42*	12.35
	0.5	D10-202	4.06	12.89
20.0	0.2	S20-201	4.13	68.21
	0.2	S20-202	2.78	73.06
	0.5	D20-201 ⁺	5.11*	27.47
	0.5	D20-202	5.04*	27.09
30.0	0.2	S30-201	3.86	120.74
	0.2	S30-202	1.04	90.75
	0.5	D30-201	4.62	45.54
	0.5	D30-202	3.13	42.43
40.0	0.2	S40-201	2.15	140.00
	0.2	S40-202	1.02	120.64
	0.5	D40-201	1.84	48.19
	0.5	D40-202	4.89	58.94

* Maximum CMOD measurable by clip gauge \approx 5.0 mm

⁺ Fracture surface image shown in Figure 10b

Table 7: Final load and crack mouth opening displacement (CMOD) values for test temperature of -40 °C

Thickness mm	a/W -	Specimen Name -	CMOD mm	Load kN
10.0	0.2	S10-401	2.45	33.95
	0.2	S10-402	0.83	26.67
	0.5	D10-401	4.50	12.11
	0.5	D10-402	1.73	11.88
20.0	0.2	S20-401	0.53	50.70
	0.2	S20-402	2.12	66.24
	0.5	D20-401 ⁺	4.56	31.31
	0.5	D20-402	1.70	24.00
30.0	0.2	S30-401	1.10	90.03
	0.2	S30-402	1.21	91.11
	0.5	D30-401	0.80	32.25
	0.5	D30-402	0.85	32.84
40.0	0.2	S40-401	2.56	139.99
	0.5	D40-401	1.28	44.88
	0.5	D40-402	0.77	41.18

⁺ Fracture surface image shown in Figure 10c

Table 8: Final load and crack mouth opening displacement (CMOD) values for test temperature of -70 °C

Thickness mm	a/W -	Specimen Name -	CMOD mm	Load kN
10.0	0.2	S10-701 ^e	1.36	32.65
	0.2	S10-702	1.64	34.21
	0.5	D10-701	0.32	9.85
	0.5	D10-702 ^a	2.61	13.85
20.0	0.2	S20-702 ^f	2.22	81.44
	0.2	S20-703	0.13	49.63
	0.5	D20-701 ⁺	0.22	20.89
	0.5	D20-702 ^c	1.09	23.95
	0.5	S20-701	1.21	26.04
30.0	0.2	S30-701 ^h	0.28	83.84
	0.2	S30-702	0.18	81.13
	0.5	D30-701 ^b	1.38	40.05
	0.5	D30-702	0.61	34.97
40.0	0.2	S40-701	0.96	129.98
	0.5	D40-701 ^d	1.19	49.87
	0.5	D40-702	0.94	48.06

Fracture surface image shown in: ⁺ Figure 10d,

^a Figure 11a, ^b Figure 11c, ^c Figure 11b, ^d Figure 11d,

^e Figure 12a, ^f Figure 12b, ^g Figure 12c.

straint samples is far greater than that of the high in-plane constraint condition. Similarly, as expected, the applied load is greater for thicker specimens.

The Charpy transition curve (Figure 5) indicates that a test temperature of $-20\text{ }^{\circ}\text{C}$ represents the cusp between the transition region and the upper shelf. Comparing Figures 8b and 9b and Table 6 shows that, regardless of initial in-plane constraint condition, identical geometries vary in terms of CMOD. This variation between identical specimen is to be expected given the statistical nature of fracture toughness testing in terms of the relationship between microstructure and transitional behaviour. In general, however, the data shows that high in-plane constraint conditions are more likely to achieve the maximum clip gauge extension compared to their low in-plane constraint counterparts. For example, in Table 6, for any given thickness comparing the lowest measured CMOD value for a high in-plane constraint condition to the highest measured CMOD value for a low in-plane constraint condition, it can be seen that the data are at least comparable if not exceeded. The single exception exists for a thickness of 40 mm, where the minimum high in-plane value (1.84 mm) is slightly below that of the maximum low in-plane value (2.15 mm).

At a test temperature of $-70\text{ }^{\circ}\text{C}$, the Charpy data indicate the approximate lower shelf. This implies that at a test temperatures of $-70\text{ }^{\circ}\text{C}$ brittle fracture mechanisms will dominate. Here one would expect that the CMOD values for identical geometries would be comparable and, for thicker specimens (where thickness $\geq 30\text{ mm}$), Figures 8d and 9d and Table 8 indicate this to be broadly the case. However, thinner specimens (i.e. thickness $\leq 20\text{ mm}$) continue to vary considerably in terms of CMOD when comparing

even identical geometries. This inconsistency does not appear to be limited to a specific in-plane constraint condition. However, more data would be required to assess whether this is a trend or whether this is simply a reflection of metallurgical effects. Similar trends were noted to occur for a test temperature of $-40\text{ }^{\circ}\text{C}$.

Comparing Figures 8a and 8d or Figures 9a and 9d shows that maximum CMOD reduces as test temperature reduces. The reduction of CMOD as temperature is reduced represents the transition from ductile behaviour (at higher temperatures) to brittle mechanisms (at lower temperatures). It is interesting to note that, regardless of initial in-plane constraint condition, on the upper shelf of the ductile-to-brittle transition (DBT) region (i.e. test temperature $\geq -20\text{ }^{\circ}\text{C}$) the maximum CMOD is comparable for each thickness investigated. At lower temperatures in the DBT (i.e. test temperatures $\leq -40\text{ }^{\circ}\text{C}$), in most cases, at least one of the thinner specimens achieve greater CMOD values when compared to their thicker counterparts. This may indicate that thinner specimens tend to be more ductile than thicker counterparts. However, it should be noted that the variability in data (when comparing identical samples at lower test temperatures) indicate that this may be a metallurgical effect as opposed to a trend. It also appears that, at low temperatures, deeply notched thin specimens ($a/W = 0.5$ and $B \leq 20\text{ mm}$) reach greater values of CMOD when compared to their shallow notched counterparts ($a/W = 0.2$ and $B \leq 20\text{ mm}$). For example, in Table 7 the CMOD for specimen D10-401 (4.5 mm) exceeds that of specimen S10-401 (2.5 mm). Similarly the CMOD of specimen D20-401 (4.6 mm) exceeds that measured for S20-402 (2.12 mm). In some cases the

CMOD obtained by these deep notched thin specimens even exceeds the CMOD measured on significantly thicker shallow notched specimen, this is shown in Table 7 when comparing measurements for D10-401 (4.5 mm) to S40-401 (2.6 mm) and, in Table 8 for specimens D10-702 (2.6 mm) to S40-701 (0.9 mm).

3.3.2. Visual inspection of samples

A visual inspection of the fracture surface of each specimen was conducted to assess the failure mode mechanisms. Figure 10 shows fracture surfaces for deeply notched ($a/W = 0.5$) 20 mm thick samples for the range of test temperatures. Figures 10a and 10b both exhibit significant plastic deformation at the fatigue pre-crack and a rough textured surface indicative of ductile tearing. In comparison Figure 10d exhibits no discernible evidence of ductile tearing or plastic deformation rather the fracture surface transitions immediately to a flat shiny type surface typical of cleavage fracture. At a test temperature of $-40\text{ }^{\circ}\text{C}$ (Figure 10c) plastic deformation and a limited amount of ductile tearing are present. The majority of crack extension (heat-tinted region) however appears to have occurred by brittle fracture. In summary the fracture surfaces shown in Figure 10 are in agreement with test data shown in Figure 8 and Tables 5 to 8 in that samples with greater amounts of ductility achieve greater values of CMOD. Additionally, as expected from load-displacement curves (Figure 8) brittle mechanisms become more dominant as test temperature decreases (i.e. ductile crack extension reduces as test temperature reduces).

As shown in Figures 5 and 10, at a test temperature of $-70\text{ }^{\circ}\text{C}$ the test material is subject to lower shelf behaviour where fracture is expected to occur in

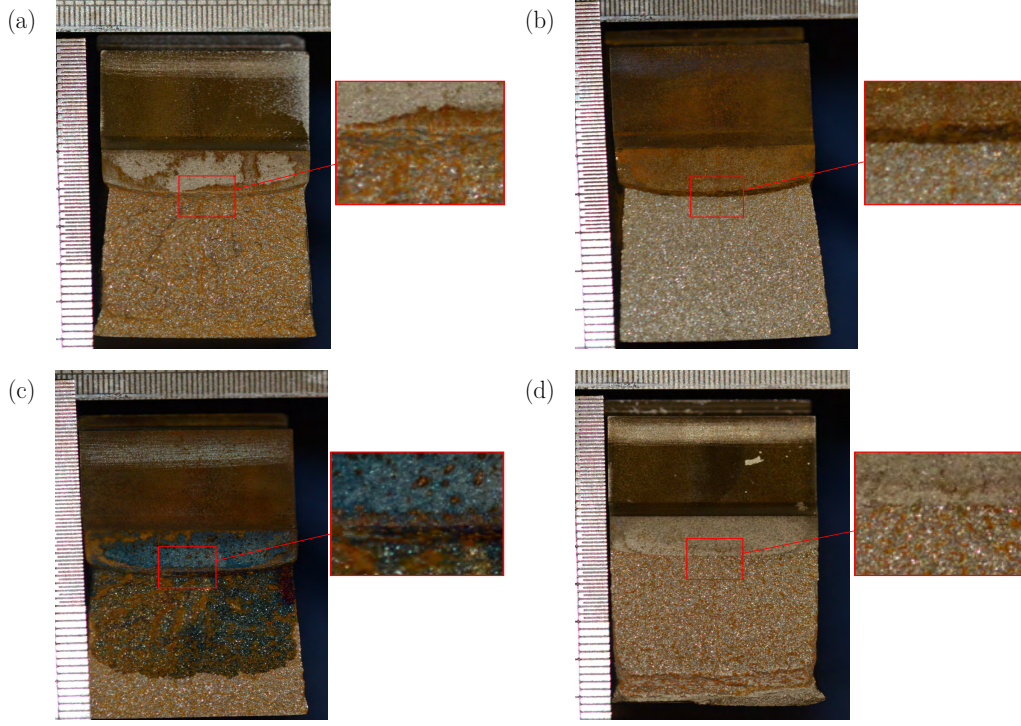


Figure 10: Fracture surfaces of deeply notched specimens with thickness of 20 mm (D20 series) tested at (a) 20 °C, (b) -20 °C, (c) -40 °C, and (d) -70 °C. Magnified regions depicting the transition from fatigue pre-crack to ductile tearing or cleavage fracture.

a predominately brittle manner. The load-displacement diagrams indicated that high in-plane constraint conditions ($a/W = 0.5$) coupled with thinner thicknesses ($10 \leq B \leq 20$ mm) potentially exhibit more ductility compared with thicker specimens (where $B > 20$ mm). Figure 11 compares the impact of out-of-plane (thickness) on the fracture surface of deeply notched specimens ($a/W = 0.5$) tested at -70 °C. Figure 11a shows that the 10 mm thick specimen exhibited significant plasticity prior to cleavage fracture as expected based on the load-displacement curve (Figure 8d). Thicker specimens (Figures 11b, 11c and 11d) failed by cleavage with no notable plastic

deformation visible on the fracture surfaces.

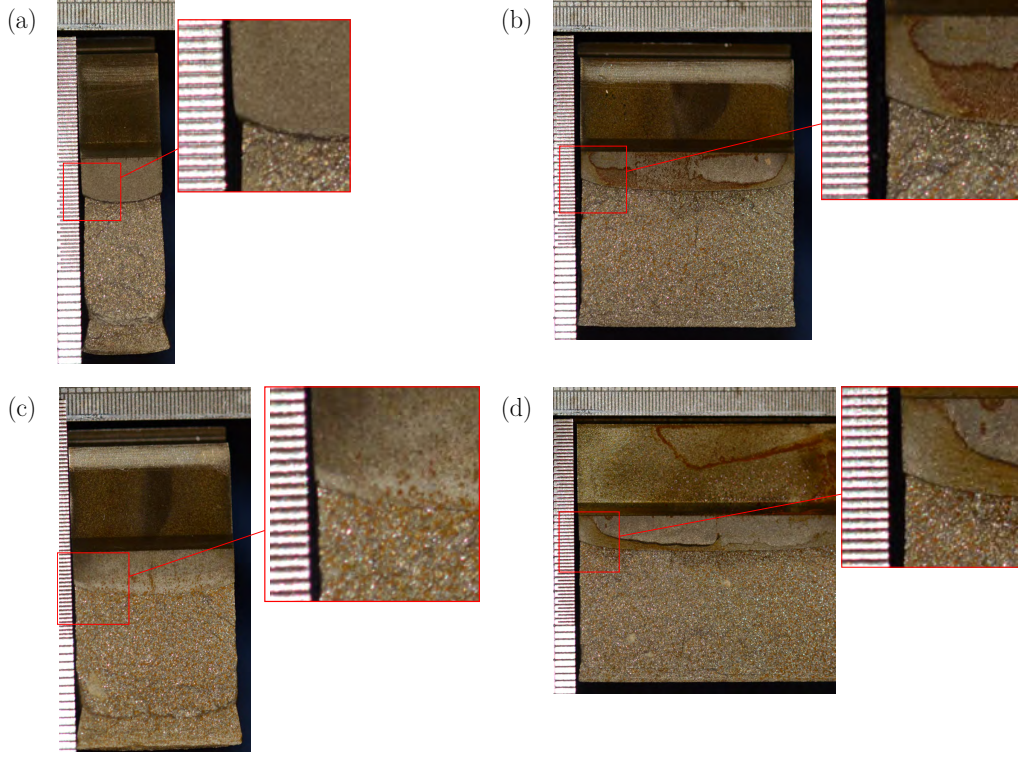


Figure 11: Fracture surfaces of deeply notched specimens ($a/W = 0.5$) tested at $-70\text{ }^{\circ}\text{C}$ for specimen thicknesses of (a) 10 mm, (b) 30 mm, (c) 20 mm, and (d) 40 mm. Magnified regions depicting the transition from fatigue pre-crack to ductile tearing or cleavage fracture.

A similar comparison is provided in Figure 12 shows the shallow notched specimens ($a/W = 0.2$) tested at $-70\text{ }^{\circ}\text{C}$. Note that Figure 12 is limited to specimen thicknesses of $B \leq 30\text{ mm}$ as the thicker specimen ($B = 40\text{ mm}$) could not be broken open at the maximum load capacity of the test machine. Figures 12a and 12c exhibit clear indications of ductile crack extension prior to brittle fracture. This plasticity is not present in Figure 12b. Fig-

ures 12a and 12b show considerable change in crack aspect ratio along the crack front with the crack length in the mid-thickness region being significantly greater than that noted at the free surface. This type of variation in crack front is often referred to as ‘*crack tunnelling*’ and is a clear indication of variation in stress triaxiality through thickness. Crack tunnelling is also indicative of a ductile failure mechanism. Deeply notched specimens of comparable thicknesses (Figures 11a and 11c) show some variation in crack aspect ratio along the crack front but, as shown in Figures 12a and 12b, reducing both in-plane and out-of-plane constraint has a compelling effect on stress triaxiality and thus failure mechanism. Figure 12c shows a comparatively flat crack profile when compared with thinner specimens. Specimens of this thickness do not exhibit any indication of ductile failure mechanism prior to cleavage. Thus the variation in failure mechanism from ductile tearing to cleavage fracture cannot be attributed purely to the in-plane constraint condition. The change in failure mechanism noted in the thinner specimens ($a/W = 0.2$, $B \leq 20$ mm Figures 11a and 11c) lends credence to the interdependency of in-plane and out-of-plane constraint and their impact on failure mechanism.

3.3.3. *Stress intensity and J-integral*

The stress intensity factor and J-integral for each specimen was calculated as outlined in the method section (Equation 13 to Equation 17). Tables 9-12 detail the calculated fracture toughness for each test temperature. As the variation between maximum applied load and failure load was considered to be small ($\approx < 1$ kN) the fracture toughness values reported were calculated at the final point of instability (i.e. at the failure load). As test temperature

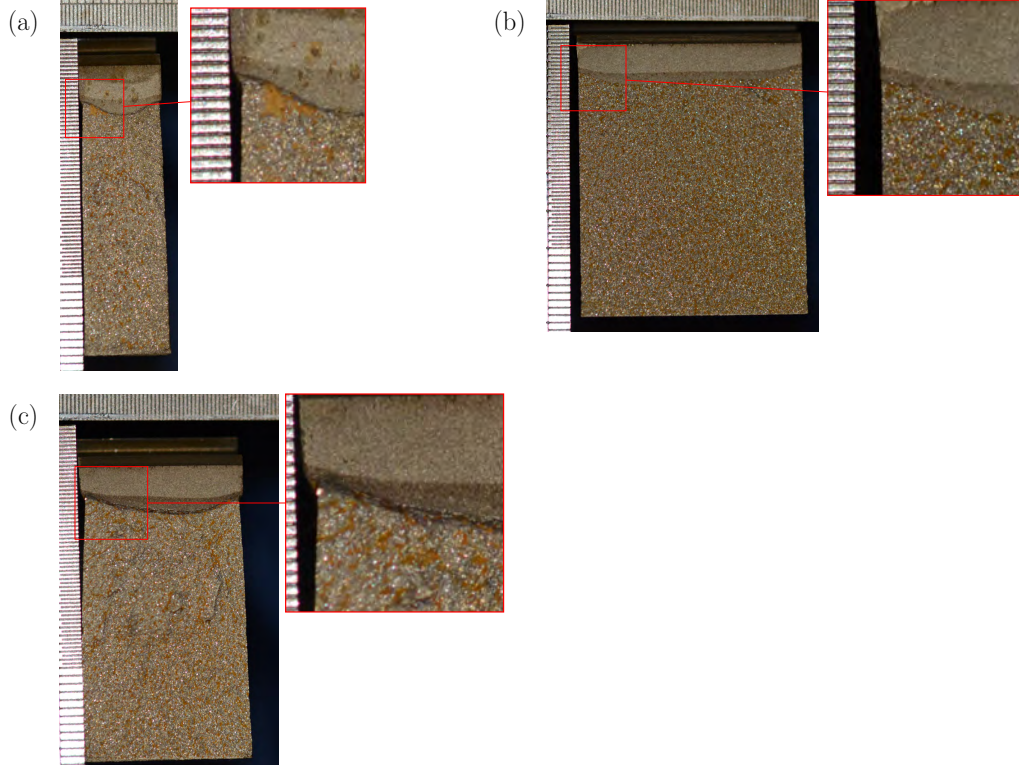


Figure 12: Fracture surfaces of shallow notched specimens ($a/W = 0.2$) tested at $-70\text{ }^{\circ}\text{C}$ for specimen thicknesses of (a) 10 mm, (b) 30 mm, and (c) 20 mm. Magnified regions depicting the transition from fatigue pre-crack to ductile tearing or cleavage fracture.

reduces, the amount of ductile tearing (Δa) was found to also, generally, reduce. This reduction in ductile tearing shows the prevalence of brittle failure mechanisms at lower test temperatures, as expected.

Tables 9-12 show that, at any given temperature, comparing specimens of similar thickness across the two in-plane conditions (e.g. ‘S10’ to ‘D10’ etc), specimens with low in-plane crack tip constraint ($a/W = 0.2$) tend to have greater magnitudes of ductile crack extension than their deeply notched counterparts for thicknesses $\leq 30\text{ mm}$. For a thickness of $B = 40\text{ mm}$

Table 9: Fracture toughness data for test temperature 20 °C. Note failure mode column specifies failure mode under which test conditions were interrupted or sample failure occurred.

ID	W	B	$\frac{a_0}{W}$	Failure mode	Failure load	Max load	J	$K_{Jc_{lt}}$	Δa	Stable tearing	Instability type
	mm	mm			kN	kN	MPam	MPa \sqrt{m}	mm		
D10RT1	40	10	0.5	Ductile	14.34	14.38	4.7	1043.46	1.03	True	Ju
D10RT2	40	10	0.5	Ductile	14.15	14.19	4.24	990.74	1.1	True	Ju
D20RT1	40	20	0.5	Ductile	29.56	29.58	3.28	869.55	0.89	True	Ju
D20RT2	40	20	0.5	Ductile	29.56	29.56	3.5	897.71	0.91	True	Ju
D30RT1	40	30	0.5	Ductile	47.17	47.17	3.65	914.94	1.0	True	Ju
D30RT2	40	30	0.5	Ductile	46.48	46.48	3.53	900.32	0.93	True	Ju
D40RT1	40	40	0.5	Ductile	59.23	59.25	2.79	797.63	0.95	True	Ju
D40RT2	40	40	0.5	Ductile	59.26	59.28	2.9	813.95	1.92	True	Ju
S10RT1 ⁺	40	10	0.2	Ductile	30.32	34.32	9.99	1519.36	4.79	True	Ju
S10RT2 ⁺	40	10	0.2	Ductile	31.86	34.57	8.9	1433.89	4.11	True	Ju
S20RT1	40	20	0.2	Ductile	78.83	78.85	6.83	1253.8	2.18	True	Ju
S20RT2	40	20	0.2	Ductile	79.8	79.8	8.0	1357.11	2.06	True	Ju
S30RT1	40	30	0.2	Ductile	124.64	124.64	7.44	1307.01	2.11	True	Ju
S30RT2	40	30	0.2	Ductile	124.95	124.96	7.04	1271.14	1.9	True	Ju
S40RT1*	40	40	0.2	Ductile	155.06	155.36	2.61	772.51	0.0	False	Jqu
S40RT2*	40	40	0.2	Ductile	159.16	159.16	4.11	969.46	0.0	False	Jqu

⁺ Significant pop-in, load-displacement curve modified in accordance with test method [26]

* Specimen not broken open. Unable to assess failure mode. J estimated assuming zero crack extension occurred.

Table 10: Fracture toughness data for test temperature -20 °C. Note failure mode column specifies failure mode under which test conditions were interrupted or sample failure occurred.

ID	W	B	$\frac{a_0}{W}$	Failure mode	Failure load	Max load	J	K_{Jc1t}	Δa	Stable tearing	Instability type
	mm	mm			kN	kN	MPam	MPa \sqrt{m}	mm		
D10-201	40	10	0.5	Ductile	12.35	12.36	4.07	994.23	0.91	True	Ju
D10-202	40	10	0.5	Brittle	12.89	12.89	2.46	774.13	0.73	True	Jqc
D20-201	40	20	0.5	Ductile	27.47	27.47	3.55	926.62	0.94	True	Ju
D20-202	40	20	0.5	Ductile	27.09	27.1	3.76	953.2	0.8	True	Ju
D30-201	40	30	0.5	Ductile	45.54	45.54	2.39	758.86	0.9	True	Ju
D30-202	40	30	0.5	Brittle	42.43	42.43	1.29	557.71	0.55	True	Jqc
D40-201	40	40	0.5	Brittle	48.19	48.2	0.48	338.06	0.3	True	Jqc
D40-202	40	40	0.5	Ductile	58.94	58.95	2.65	796.25	1.32	True	Ju
S10-201 ⁺	40	10	0.2	Brittle	32.6	32.61	1.44	592.63	0.44	True	Jqc
S10-202	40	10	0.2	Brittle	34.73	34.75	3.53	926.37	0.98	True	Jqc
S20-201	40	20	0.2	Brittle	68.21	68.22	4.96	1095.14	2.48	True	Jqc
S20-202	40	20	0.2	Brittle	73.06	73.07	2.45	770.15	1.11	True	Jqc
S30-201	40	30	0.2	Brittle	120.74	120.76	4.21	1006.78	1.25	True	Jqc
S30-202	40	30	0.2	Brittle	90.75	90.75	0.45	329.64	0.38	True	Jqc
S40-201 [*]	40	40	0.2	-	140.0	140.0	1.47	591.94	0.0	False	Jc
S40-202	40	40	0.2	Brittle	120.64	120.64	0.4	307.54	0.38	True	Jqc

⁺ Significant pop-in, load-displacement curve modified in accordance with test method [26]

^{*} Specimen not broken open. Unable to assess failure mode. J estimated assuming zero crack extension occurred.

Table 11: Fracture toughness data for test temperature -40 °C. Note failure mode column specifies failure mode under which test conditions were interrupted or sample failure occurred.

ID	W	B	$\frac{a_0}{W}$	Failure mode	Failure load	Max load	J	$K_{J_{crit}}$	Δa	Stable tearing	Instability type
	mm	mm			kN	kN	MPam	MPa \sqrt{m}	mm		
D10-401 ⁺	40	10	0.5	Brittle	12.11	12.11	2.07	702.7	0.58	True	Jqc
D10-402	40	10	0.5	Brittle	11.88	11.9	0.49	342.47	0.0	False	Jc
D20-401	40	20	0.5	Brittle	31.31	31.31	2.68	795.71	0.55	True	Jqc
D20-402	40	20	0.5	Brittle	24.0	24.09	0.49	340.24	0.0	False	Jc
D30-401	40	30	0.5	Brittle	32.25	32.39	0.13	176.8	0.11	False	Jc
D30-402	40	30	0.5	Brittle	32.84	32.84	0.14	181.21	0.0	False	Jc
D40-401	40	40	0.5	Brittle	44.88	44.88	0.26	244.71	0.0	False	Jc
D40-402	40	40	0.5	Brittle	41.18	41.18	0.1	147.5	0.0	False	Jc
S10-401	40	10	0.2	Brittle	33.95	33.95	1.83	660.77	0.74	True	Jqc
S10-402	40	10	0.2	Brittle	26.67	26.68	0.29	264.44	0.45	True	Jqc
S20-401	40	20	0.2	Brittle	50.7	50.7	0.16	194.47	0.58	True	Jqc
S20-402	40	20	0.2	Brittle	66.24	66.24	1.51	598.24	0.92	True	Jqc
S30-401	40	30	0.2	Brittle	90.03	90.03	0.52	349.17	0.23	True	Jqc
S30-402	40	30	0.2	Brittle	91.11	91.12	0.62	380.04	0.13	False	Jc
S40-401 [*]	40	40	0.2	-	139.99	139.99	2.29	732.57	0.0	False	Jc

⁺ Significant pop-in, load-displacement curve modified in accordance with test method [26].

^{*} Specimen not broken open. Unable to assess failure mode. J estimated assuming zero crack extension occurred.

Table 12: Fracture toughness data for test temperature -70 °C. Note failure mode column specifies failure mode under which test conditions were interrupted or sample failure occurred.

ID	W	B	$\frac{a_0}{W}$	Failure mode	Failure load	Max load	J	$K_{J_{crit}}$	Δa	Stable tearing	Instability type
	mm	mm			kN	kN	MPam	MPa \sqrt{m}	mm		
D10-701	40	10	0.5	Brittle	9.85	9.85	0.02	69.51	0.04	False	Jc
D10-702	40	10	0.5	Brittle	13.85	13.85	1.22	532.07	0.64	True	Jqc
D20-701	40	20	0.5	Brittle	20.89	20.89	0.02	67.42	0.0	False	Jc
D20-702	40	20	0.5	Brittle	23.95	23.96	0.25	240.45	0.0	False	Jc
D30-701	40	30	0.5	Brittle	40.05	40.05	0.29	256.14	0.0	False	Jc
D30-702	40	30	0.5	Brittle	34.97	34.97	0.07	122.43	0.0	False	Jc
D40-701	40	40	0.5	Brittle	49.87	49.87	0.17	193.95	0.04	False	Jc
D40-702	40	40	0.5	Brittle	48.06	48.06	0.15	179.46	0.0	False	Jc
S10-701	40	10	0.2	Brittle	32.65	32.65	0.94	466.55	0.37	True	Jqc
S10-702	40	10	0.2	Brittle	34.21	34.21	0.94	468.28	0.54	True	Jqc
S20-701	40	20	0.5	Brittle	26.04	26.04	0.27	247.22	0.0	False	Jc
S20-702	40	20	0.2	Brittle	81.44	81.44	1.42	569.77	0.59	True	Jqc
S20-703	40	20	0.2	Brittle	49.63	49.63	0.0	11.09	0.12	False	Jc
S30-701	40	30	0.2	Brittle	83.84	83.84	0.08	131.08	0.0	False	Jc
S30-702	40	30	0.2	Brittle	81.13	81.13	0.03	85.24	0.0	False	Jc
S40-701*	40	40	0.2	-	129.98	129.98	0.39	293.95	0.0	False	Jc

* Specimen not broken open. Unable to assess failure mode. J estimated assuming zero crack extension occurred.

however, the deeply notched specimens tend exhibit more ductile tearing.

Figure 13 plots the fracture toughness as a function of ductile crack extension for specimens with a high in-plane constraint condition and thicknesses of (a) 10 mm, (b) 20 mm, (c) 30 mm, and (d) 40 mm. The data for each thickness were then assessed using linear regression to give an indication of the effect of thickness. Using the regression line the J at initiation ($J_{IC}^* = J$ at $\Delta a = 0.2$ mm) was estimated. The lowest J_{IC}^* ($0.57 \text{ MPa}\sqrt{m}$) occurred when $B = 40$ mm, this is not unexpected as this sample geometry represents the most highly constrained crack tip parameters. Regression data associated with each curve in Figure 13 are given in Table 13

A similar study was conducted for specimens with low in-plane constraint as detailed in Figure 14. Some low in-plane constraint specimens, particularly thinner specimens, had significant amounts of ductile tearing prior to cleavage. Considering the use of linear regression rather than curve fitting, only data where $\Delta a \leq 2.5$ mm were analysed. As ductile crack extension could not be analysed on all specimen thicknesses of $B = 40$ mm, regression analysis was not conducted for this thickness. Regression data associated with other thicknesses (i.e. $B \leq 30$ mm) in Figure 14 are provided in Table 13.

Figure 15a compares the regression data for each thickness for high in-plane constraint condition ($a/W = 0.5$). As shown the slope of the R-curve reduces as specimen thickness increases, this is as expected and is agreement with literature. Broadly Figure 15a shows that thickness effects are minimal for specimen thicknesses $B \leq 30$ mm. For low in-plane crack tip constraint conditions, see Figure 15b, similar results were noted.

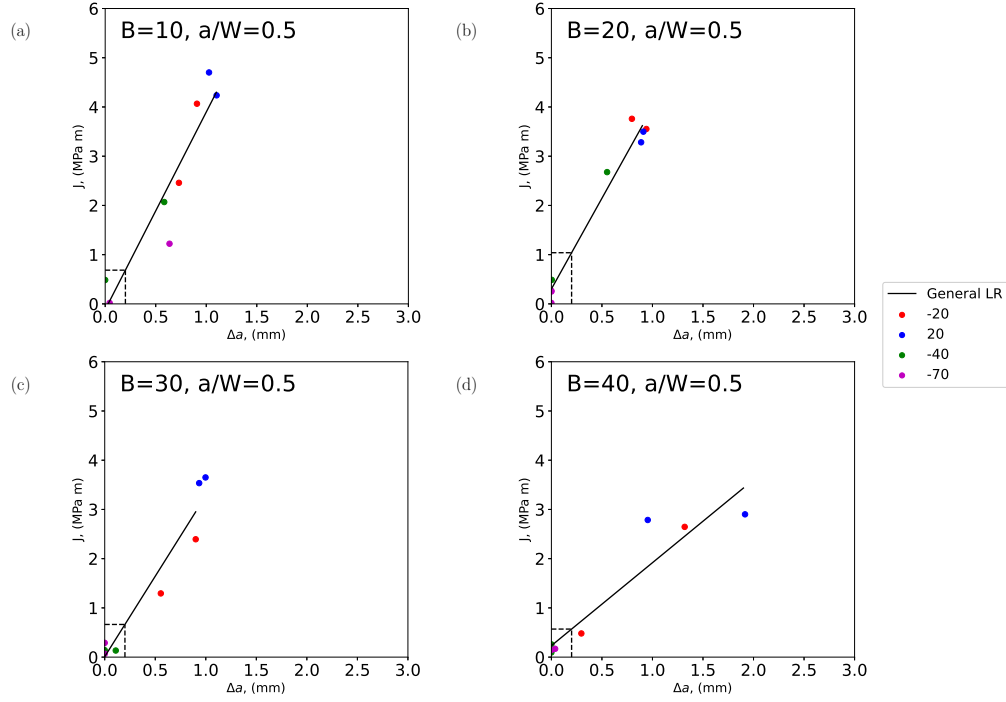


Figure 13: J versus ductile crack extension Δa for high in-plane constraint ($a/W = 0.5$) condition for each specimen thickness investigated (a) 10 mm, (b) 20 mm, (c) 30 mm, and (d) 40 mm. Points present the ductile tearing results at various test temperatures at which cleavage intervenes.

The crack driving force was calculated using Equation 18, where the appropriate value of Young's modulus, E , was taken from Table 4, and is plotted as a function of temperature and specimen thickness in Figure 16 for (a) high in-plane constraint and (b) low in-plane constraint conditions. Linear regression was performed on data to illustrate trends attributed to out-of-plane constraint condition. The overall shape of the curves presented in Figure 16 are relevant only to temperatures in the DBT region. These data are extrapolated beyond the DBT in Figure 16 purely for illustrative

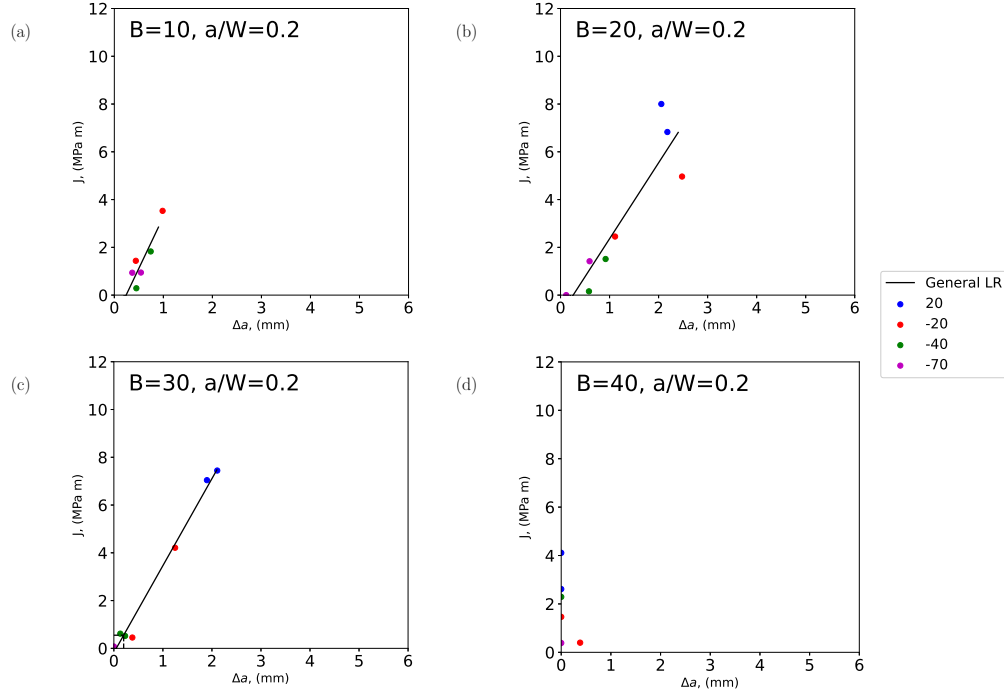


Figure 14: J versus ductile crack extension Δa for low in-plane constraint ($a/W = 0.2$) condition for each specimen thickness investigated (a) 10 mm, (b) 20 mm, (c) 30 mm, and (d) 40 mm. Points present the ductile tearing results at various test temperatures at which cleavage intervenes.

purposes.

Figure 16 shows, as expected, an increase in crack driving force as temperature increases. Under high in-plane constraint ($a/W = 0.5$), for comparable temperatures, thicker specimens (higher out-of-plane constraint) reduces crack driving force at the crack tip (see Figure 16a). Under low in-plane constraint ($a/W = 0.2$), see Figure 16b, a similar trend in crack driving force and thickness was noted to occur. The slope of the curve associated with 40 mm thick specimens differs considerably compared with other specimen thick-

Table 13: Linear regression data for fitting J versus Δa where Δa is limited to maximum of 2.5 mm and y-intercept is assumed to be zero. Regression data calculated based on points shown in Figures 13 and 14.

Data from	a/W	Thickness	Slope	Intercept	R^2	MSE*	J_{IC}^*
	-	mm	-	MPam	-	-	MPam
Figure 13	0.2	10.0	4.32	-1.04	0.81	0.20	-0.18
		20.0	3.18	-0.82	0.82	1.45	-0.18
		30.0	3.64	-0.18	0.99	0.11	0.55
Figure 14	0.5	10.0	4.01	-0.12	0.88	0.35	0.68
		20.0	3.69	0.30	0.97	0.07	1.04
		30.0	3.27	0.01	0.93	0.14	0.66
		40.0	1.69	0.23	0.89	0.17	0.57

* Mean squared error

nesses. This change in slope is attributed to two factors: 1. The assumed zero ductile crack growth in room temperature tests (ductile crack growth could not be measured) impacting the calculation of J_{pl} (Equation 16) and thus the calculation of K_{Jc} (Equation 18), and, 2. The specimen thickness approaching the thickness plateau where further increases to thickness no longer impacts fracture toughness [31]. Table 14 shows the linear regression data. As shown, and as expected considering the number of samples and variability of data, the R^2 value is low while the mean squared error is large. These statistical scores reflect the variability of test data.

Figure 16 generally shows that, regardless of in-plane constraint condition, increasing out-of-plane constraint (thickness) reduces crack driving

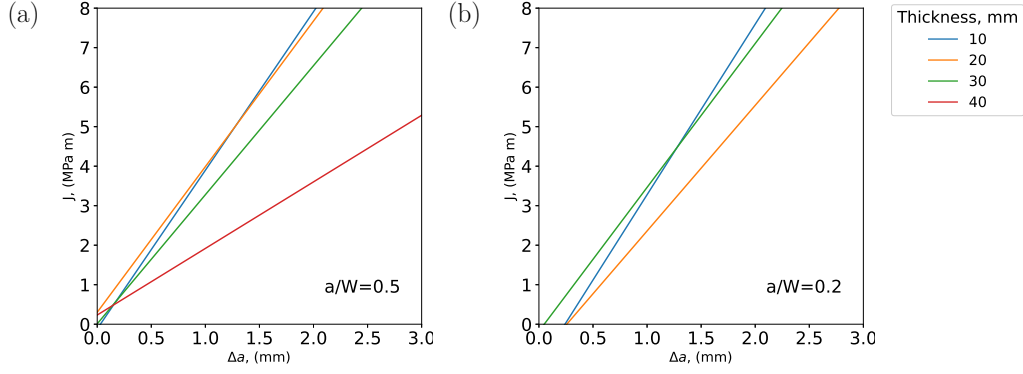


Figure 15: Comparison of R-curves for each specimen thickness showing (a) high in-plane constraint ($a/W = 0.5$) and (b) low in-plane constraint ($a/W = 0.2$). Derived using parameters shown in Table 13.

force. Anderson [31] provides a good discussion on how this trend “reflects the differing relative contributions of two distinct fracture mechanisms” and is supported by fracture surface images gathered as part of this work (see Figures 10, 11 and 12). The thickness effect shown in Figure 16 also supports the current pressure vessel design codes (e.g. PD 5500 Annex D [5] and EN 13445 Annex B [8]), which account for thickness effects through the use of multiple thickness design curves. The design curves simply describe a relationship between pressure vessel operating temperature and Charpy impact toughness test temperature. Assuming the minimum Charpy energy requirement can be demonstrated (i.e. 27 J or 41 J at a Charpy test temperature), the minimum operating temperature of the pressure vessel can be derived using the appropriate design curve (i.e. the appropriate curve for the materials yield strength and the specific pressure vessel wall thickness). It should be noted that the design curves in PD 5500 penalise users, for increases in pressure vessel thickness, to a much greater extent than EN 13445.

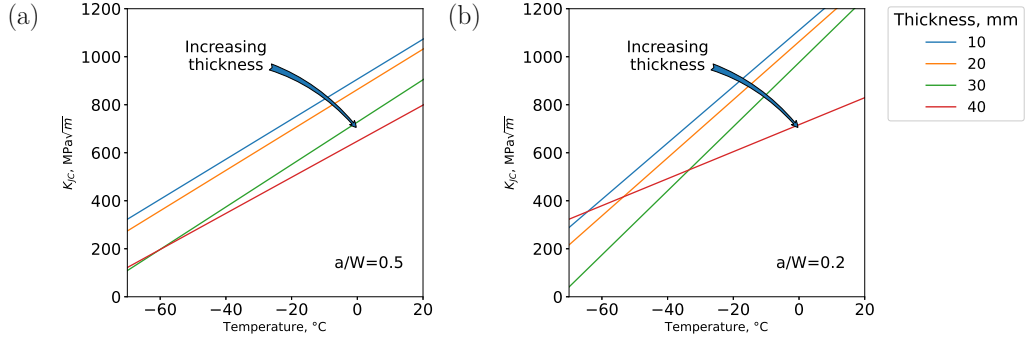


Figure 16: Comparison of K_{Jc} versus temperature for each specimen thickness showing (a) high in-plane constraint ($a/W = 0.5$) and (b) low in-plane constraint ($a/W = 0.2$)

Figure 16 would indicate that the thickness effect applied to design curves in EN 13445 are more appropriate than that adopted to PD 5500.

Table 14: Parameters for linear regression fit shown in Figure 16.

a/W	Thickness	Slope	Intercept	R^2	MSE
-	mm	-	$\text{MPa}\sqrt{\text{m}}$	-	-
0.2	10.0	11.74	1110.23	0.78	40840.15
	20.0	12.10	1062.68	0.76	49805.63
	30.0	13.35	975.60	0.85	32481.63
	40.0	5.62	716.85	0.53	28312.51
0.5	10.0	8.33	906.19	0.70	31429.01
	20.0	8.42	863.12	0.69	35142.08
	30.0	8.83	727.35	0.83	17675.81
	40.0	7.52	648.11	0.74	21727.08

3.3.4. Estimating T_0 from fracture toughness data

The T_0 of the material was previously estimated using Charpy impact testing to be in the temperature range of $-60^\circ\text{C} \leq T_0 \leq -68^\circ\text{C}$ (see Table 3). Following guidance [23] specimens tested at -70°C (i.e. Table 12) were further analysed to achieve a better approximation of T_0 as outlined in the method section.

The test method [23] for calculating T_0 specifies the use of standard specimen geometries only, e.g. the initial crack aspect ratio should be $a/W \geq 0.5$ with thicknesses limited to $B = 0.5W$ or $B = W$. In this work removing non-standard out-of-plane and in-plane geometries results in only five uncensored data points, where the test method requires a minimum of six uncensored data for T_0 estimation. Table 15 provides results for several considered sub-data sets. The first column in Table 15 uses specimens that meet the required in-plane and out-of-plane conditions as specified in the test method. In order to increase the data set size standard out-of-plane thicknesses, regardless of in-plane constraint condition, were also investigated, results are shown in the second column of Table 15. In the first instance, where we rigidly adopt standard guidelines, T_0 is estimated to be $\approx -115^\circ\text{C}$. When in-plane constraint conditions are disregarded (second column of Table 15) the dataset increases to eight uncensored data with an estimated T_0 of -146°C . This $\approx 30^\circ\text{C}$ decrease in T_0 is considered relatively significant and clearly demonstrates that the higher magnitudes of toughness measured on shallow notched geometries ($a/W = 0.2$) effect the calculation of T_0 .

In the final two columns of Table 15 the effect, on T_0 , of disregarding thickness is investigated. As shown, when the out-of-plane requirement is

Table 15: Estimated T_0 value for specimens tested at -70°C considering both out-of-plane and in-plane constraint conditions.

Units	Out-of-plane:	$B \times B$ and $B \times 2B$		All thicknesses	
		$a/W \geq 0.5$	$a/W \geq 0.2$	$a/W \geq 0.5$	$a/W \geq 0.2$
-	N	5.00	8.00	9.00	16.00
-	r	5.00	8.00	9.00	16.00
$\text{MPa}\sqrt{m}$	K_0	210.48	356.85	323.54	373.63
$\text{MPa}\sqrt{m}$	$K_{Jc_{med}}$	193.80	327.36	296.97	342.67
$^\circ\text{C}$	T_0	-114.75	-146.13	-140.45	-148.77

disregarded but the in-plane requirement is maintained (i.e. $a/W \geq 0.5$) the T_0 is estimated to be $\approx -140^\circ\text{C}$. As noted earlier thinner specimens appeared to be more ductile than thicker counterparts. In this regard the downward shift in T_0 is not wholly unexpected in terms of the data investigated here but, the downward shift in T_0 indicates that out-of-plane constraint, which is generally considered to be of less importance than in-plane constraint, also influences T_0 estimations significantly. It should be noted that for this case there are enough uncensored data to fulfil the test method requirements. These results indicated that the use of non-standard SENB thicknesses can result in unconservative measures of T_0 and thus the use of non standard geometries should be handled cautiously. The lowest estimation of $T_0 \approx -150^\circ\text{C}$ was found, unsurprisingly, to occur when both in-plane and out-of-plane requirements were disregarded.

While an exact measure of T_0 cannot be discerned from the data it is

considered likely to lie in the range $-115 \leq T_0 \leq -140^\circ \text{ C}$.

The standard deviation associated with the Weibull distribution was calculated as a function of median toughness, $K_{Jc_{med}}$, from Equation 23 [23]. Considering a high in-plane constraint condition ($a/W = 0.5$) it is shown here that for standard and non-standard thicknesses the standard deviation to be $\pm 48.63 \text{ MPa}\sqrt{m}$ and $\pm 77.55 \text{ MPa}\sqrt{m}$, respectively. Using Equation 22 the range of T_0 values associated with the standard deviation of $K_{Jc_{med}}$ were calculated, results are provided in Table 16.

Table 16: Standard deviation of median toughness $K_{Jc_{med}}$ for high in-plane constraint condition $a/W = 0.5$. Estimated range of T_0 for given standard deviation.

Out-of-plane:	units	$B \times B$ and $B \times 2B$	All thicknesses
$K_{Jc_{med}}$		193.80	296.97
σ	$\text{MPa}\sqrt{m}$	48.63	77.55
Minimum $K_{Jc_{med}} = K_{Jc_{med}} - \sigma$		145.06	219.40
Maximum $K_{Jc_{med}} = K_{Jc_{med}} + \sigma$		242.32	374.50
T_0 for minimum $K_{Jc_{med}}$	$^\circ \text{ C}$	-108.35	-130.13
T_0 for maximum $K_{Jc_{med}}$		-135.36	-158.27

Figure 17 plots the master curve for (a) $T_0 = -115^\circ \text{ C}$ and (b) $T_0 = -140^\circ \text{ C}$. Test data points are included for comparative purposes only, readers should refer to Table 15 for specific information related to specimens used in the calculation. The upper (UB) and lower (LB) tolerance bounds shown in Figure 17 were calculated using Equation 24 where C represents

the 5 % and 95 % confidence in T_0 . As expected Figure 17a better approximates the minimum toughness values measured experimentally compared to Figure 17b. Note that specimens outside the lower bound of Figure 17a are shallow notched ($a/W = 0.2$) specimens and non-standard specimen thicknesses. To prevent brittle fractures accurately predicting minimum fracture toughness measurements is vital thus, for structural integrity assessments, Figure 17a and a $T_0 = -115$ °C is considered more appropriate.

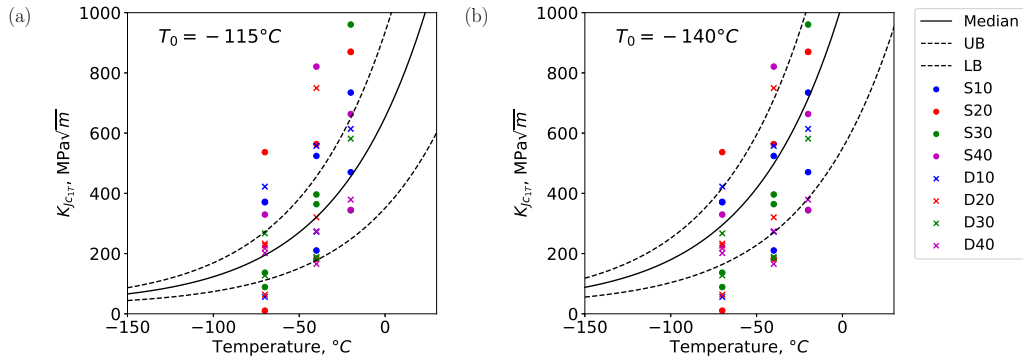


Figure 17: Master curve relationship using test data subsets at -70°C: (a) in-plane and out-of-plane requirements (Table 15, column one), (b) in-plane requirements only (Table 15, column three). Scatter data points for all test temperatures -70 °C, -40 °C and -20 °C shown for comparison only.

3.3.5. Additional noteworthy events

Significant pop-in events were noted to occur in four fracture specimens, the fracture surfaces are shown in Figure 18 where the localised brittle zones (LBZs) are identified in magnified regions. Interestingly these pop-in events appear predominately in specimens with combined low in-plane and out-of-plane constraint conditions (e.g. S10 series), generally occurring in the mid-thickness region at the fatigue pre-crack tip at higher test temperatures

(≥ -20 °C). What is interesting here, is how limited the regions containing evidence of brittle fracture mechanisms are compared to ductile regions. Steel manufacturing processes have developed significantly in recent decades and one notable improvement has been better control over the distribution, location, size and composition of non-metallic inclusions [32]. Non-metallic inclusions have been shown to be of key importance in regards to failure mechanisms [33, 34, 35]. The results found in this work imply that this material has few non-metallic inclusions or is a relatively “clean” material. Materials produced using other manufacturing processes, or welded materials, would likely exhibit significantly more pop-in events than seen for this material.

The presence of these LBZs implies that high triaxiality exists in the mid-thickness region. High triaxiality in the mid-thickness has been well documented [31]. Pineau et al. [36] provides an overview of dependencies influencing fracture stress. They state that there are three main contributions to fracture: 1. Work in the fracture process zone, 2. Work associated with necking and, 3. Work associated with gross plastic dissipation. For thin sheets, competition between brittle (flat) and slant (ductile tearing related to shear stresses) fracture, results not only in complex crack paths but also increasing fracture contributions due to necking. Thinner thicknesses give rise to plane stress conditions in the fracture process zone which increases necking in the region. Thus, in thinner specimens, **large amounts of ductile damage may occur in the fracture processes zone prior to crack initiation at the crack tip**. Regions of high triaxiality (i.e. the mid-thickness) is likely to incur greater void formation. It is postulated that,

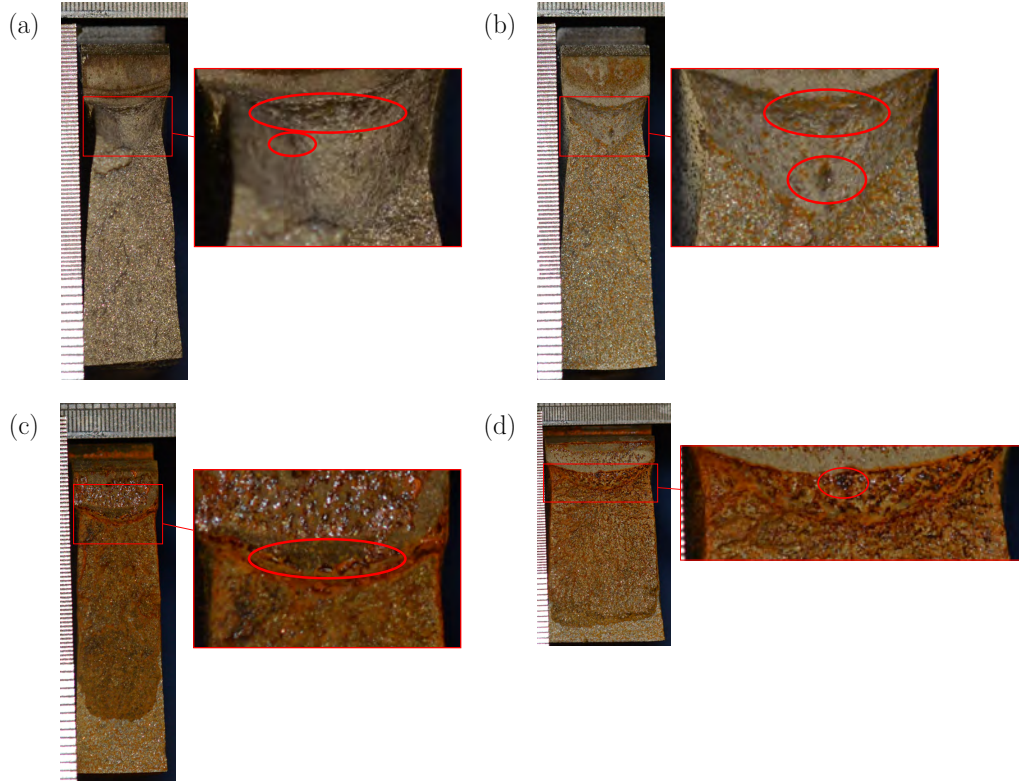


Figure 18: Fracture surface of specimens exhibiting pop-in behaviour (a) S10RT1: Magnified image showing substantial local brittle zone (LBZ) followed by significant ductile deformation and a second significant pop-in. (b) S10RT2: Magnified image showing fracture surface similar to that noted in (a) with a LBZ at the a_o followed by ductile fracture and a second significant pop-in. (c) S10-401: LBZ occurring at a_o followed by mixed mode fracture mechanisms. and (d) S20-201: Relatively small local brittle zone occurring at a_o followed by significant ductile tearing subsequent failure predominately occurring via brittle fracture mechanisms.

the ductile damage in the fracture process zone, may be of such magnitude that it is comparable to a crack like environment. Thus “In this case the first coalescence events do not necessarily occur with the crack tip” [36]. It is possible that these LBZ’s may have formed after ductile damage in fracture process zone has reached some critical value. In this case small regions, in the mid-thickness close to the crack tip, may incur high crack tip constraint conditions inducing brittle fracture. This would explain why these events are limited to thinner specimens and do not occur in thicker counterparts. Given the small sample size however, the relationship between significant pop-in events and crack tip constraint cannot be discerned from the existing test data.

3.4. Finite element modelling

3.4.1. Estimating plastic collapse load

The plastic collapse load for each model geometry was derived from elastic-plastic simulations described previously (see Section 2.4.1). Results are tabulated in Table 17 for the various crack tip constraints investigated.

3.4.2. Calculating T-stress for a 2D linear-elastic condition

Linear-elastic FEM models for both 2D plane stress and plane strain conditions were investigated. The T-stress was found to be identical when plane stress or plane strain conditions were assumed. Results for the plane strain condition are shown in Table 18. For specimens with thicknesses $B \geq 20$ mm Table 18 shows the T-stress to be identical, for specific in-plane constraint conditions. This is as expected given that out-of-plane constraint cannot be adequately addressed under 2D assumptions. A slight deviation

Table 17: Plastic collapse load from elastic-plastic 2D simulations

B mm	Plastic Collapse Load	
	kN	
	$a/W = 0.2$	$a/W = 0.5$
10	15.01	8.22
20	31.30	16.35
30	46.95	24.52
40	62.60	32.69

was noted to occur for specimens assigned a thickness of 10 mm. Considering the variance is less than 5 MPa and given that standard deviation remains within 0.02 MPa of the mean value, the change is considered to be negligible.

3.4.3. Calculating *T*-stress for a 3D linear-elastic condition

To adequately capture *T*-stress variations due to out-of-plane (thickness) effects, 3D linear-elastic finite element modelling was conducted. Table 19 shows the maximum standard deviation of *T*-stress across contours 2 to 20 for any thickness position. As shown the maximum standard deviation is 0.07 MPa indicating good contour convergence, hence path independence of the contour integral can be assumed.

To compare *T*-stress from the 2D analyses with the 3D analyses, *T*-stresses in the 3D analyses were also averaged across the specimen thickness. This provides a single *T*-stress value representative of the specific crack tip constraint condition. As shown in Table 20 the standard deviation reduces as specimen thickness increases. It is well understood that plane stress con-

Table 18: Standard deviation and average T-stress values for 2D LE analyses across contours 2:20.

B	$a/W = 0.2$		$a/W = 0.5$	
	Std dev	T-stress	Std dev	T-stress
mm	MPa			
10		-105.87		43.34
20	0.01		0.02	
30		-110.42		43.03
40				

ditions begin to affect stress distribution through thickness within 1-2 mm of the sample surface [31]. Considering our sample thicknesses, if we assume plane stress conditions to be prevalent within 1 mm of the surface then the percentage area effect is $(2/10) \times 100 = 20\%$. In a thicker sample, say 40 mm, the percentage area affected by plane stress conditions is reduced to $(2/40) \times 100 = 5\%$. This effect is seen in Table 20 for thin samples where the standard deviation, which is dependent on the number of measurements or, in this case the number of elements through thickness, is notably larger compared to thicker samples.

Figure 19 shows the normalised T-stress distribution for each in-plane and out-of-plane crack tip condition. Here we have normalised T-stress with bending stress. For each thickness and a/W ratio, the T-stress distribution through the thickness was normalised using the MinMaxScaler method [37]. As shown, regardless of in-plane or out-of-plane condition, elements adjacent to the outer surface of the specimen have stresses that differ significantly from

Table 19: Maximum standard deviation of T-stress values for 3D LE analyses averaging across contours 2:20. Values provided are the maximum considering all thickness positions.

B	$a/W = 0.2$	$a/W = 0.5$
mm	MPa	
10	0.07	0.07
20	0.07	0.07
30	0.07	0.06
40	0.06	0.06

those located at the mid-thickness. While removing these elements from the stress distribution would undoubtedly reduce the standard deviation it would result in an inaccurate measure of general thickness related T-stress because plane stress conditions also affect real world test samples. Considering that the purpose of these 3D models is to address shortfall's in the 2D assumption, it was decided to maintain the outliers in the averaging process.

The variation in T-stress through the specimen thickness is shown for the low in-plane constraint condition, Figure 20a and the high in-plane constraint condition, Figure 20b. The 2D plane strain T-stresses are included for comparison. As shown in Figure 20 some variability occurs at nodes along the thickness path. It is key here to note that finite element simulations calculate stresses and strains at integration points **not** at nodal positions. The integration point values are extrapolated, by averaging, to nodal positions. In cases where there is a large gradient, such as that expected as plane stress conditions start to dominate, variability at nodal positions is to be expected. This is shown clearly in Figure 20b, where nodal position values

Table 20: Average and standard deviation of T-stress when averaging through thickness for 3D finite element analyses.

B	$a/W = 0.2$		$a/W = 0.5$	
	Std dev	T-stress	Std dev	T-stress
mm	MPa			
10	16.13	-42.98	16.34	34.39
20	8.98	-51.05	9.19	30.67
30	6.76	-53.99	8.16	28.53
40	6.08	-55.65	7.39	26.81

vary considerably close to the outer surface and are converge as the mid-thickness is approached. Figure 20 shows that the averaged T-stress through the specimen thickness for the 3D models is slighted reduced when compared to T-stress calculated from the 2D assumption.

Negative T-stresses are generally associated with a loss of constraint [38, 22, 1, 39]. As shown in Table 21 columns 2 & 4, high in-plane constraint conditions, where $a/W = 0.5$, result in positive measures of T-stress indicating no loss of constraint, as would be expected. Investigating column 2 in more detail, however, shows that while T-stress remains positive for all cases, increases in specimen thickness **reduce** the measured value of T-stress. The reduction in T-stress is minimal (approximately 2 MPa per 10 mm thickness increase) and, for the thickest specimen investigated, $B = 40$ mm, the measured T-stress is still overwhelmingly positive at ≈ 27 MPa.

This trend of increasing specimen thickness resulting in a reduction of constraint is in direct contradiction to the general theory that increases in

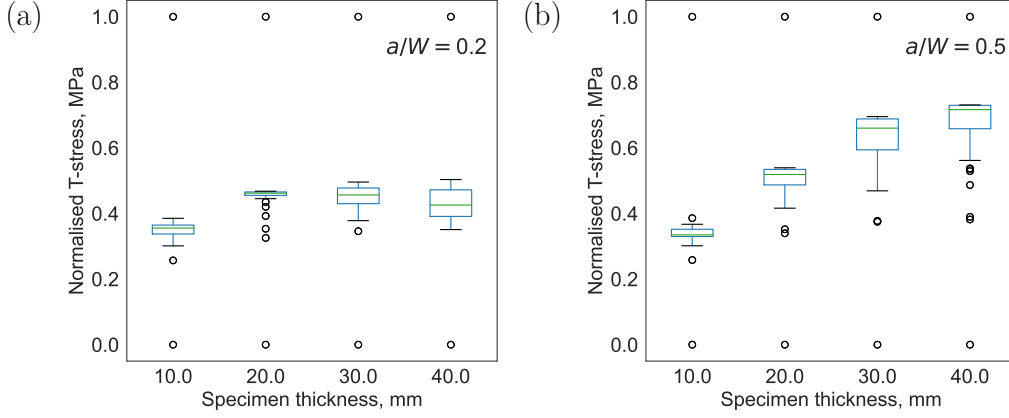


Figure 19: Normalised T-stress variation through thickness for (a) low in-plane constraint $a/W = 0.2$ conditions and (b) high in-plane constraint $a/W = 0.5$ conditions.

thickness and/or increases to notch depth induce higher constraint conditions on the crack tip. However, it is important to highlight at this point the geometrical conditions under which this work was conducted. Here we have used a set value of specimen width ($W = 40$ mm) so only two of the four FE simulations adhere to standard geometrical guidelines. For a $B = 10$ mm the width, according to test method guidance, should be $W = 10$ mm or $W = 20$ mm (depending on whether samples are of $B \times B$ or $B \times 2B$ type). Similarly the expected width for a $B = 30$ mm specimen would be $W = 30$ mm or $W = 60$ mm. The T-stress is a uniform stress parallel to the plane of the crack which induces a stress in the thickness direction. In fact, T-stress can be scaled directly from stress intensity factor via a biaxiality ratio (Equation 25) both are strongly impacted by specimen geometry [40, 31]. Hence this unexpected trend of increasing specimen thickness resulting in a reduction of constraint is considered a function of the variability in the biaxiality ratio.

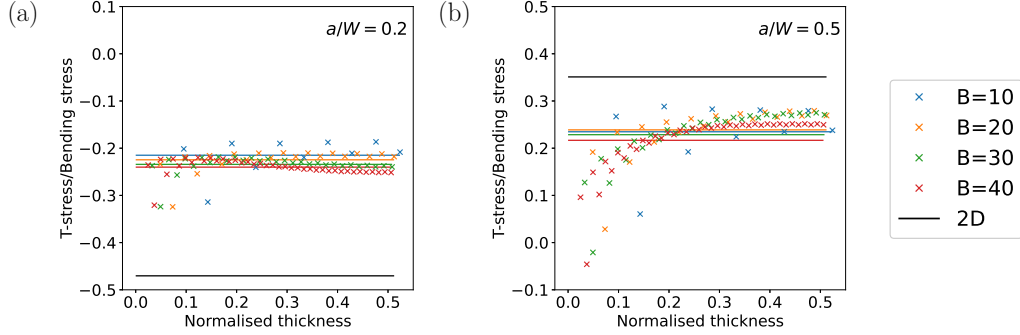


Figure 20: T-stress variation through normalised thickness from surface (0.0) to mid-thickness (0.5) region at the point of plastic collapse for (a) low in-plane constraint $a/W = 0.2$ conditions and (b) high in-plane constraint $a/W = 0.5$ conditions. The average T-stress through the section is shown for comparison purposes. Notes: 1. y-axis limits are not identical, 2. As the model is linear-elastic results are scalable to other points of interest (e.g. yield strength).

$$\beta = T\sqrt{\pi a}/K_I \quad (25)$$

Considering low in-plane constraint conditions, where $a/W = 0.2$, in Table 21 column 1 it is shown that T-stress is negative. This is as expected and is again in agreement with literature. Moreover it shows that for shallow notches a loss of constraint should be expected. Similar to the trend noted previously results for the shallow notch also show that increasing specimen thickness results in increasingly negative measures of T-stress. As shown in both Figures 20a and 20b T-stress values close to the free surface were found to be more negative than those occurring in the mid-thickness region, this is as expected and demonstrates a loss of constraint at the free surface.

Comparing the 2D and 3D T-stress results for a low in-plane constraint condition (Figure 20a), it is shown that the 2D analysis is approximately

Table 21: T-stress at plastic collapse load. 3D simulation results averaged over 18 contours and through thickness. 2D simulation results averaged over 18 contours.

T-stress, MPa				
B (mm)	3D		2D PE	
	$a/W = 0.2$	$a/W = 0.5$	$a/W = 0.2$	$a/W = 0.5$
10	-45.50	32.03		
20	-51.08	30.64		
30	-53.84	28.62	-110.42	43.03
40	-55.52	26.88		

twice that predicted for a 3D analysis of comparable thickness. This is not unexpected given that 2D geometries do not account for out-of-plane variations (i.e. there is no thickness effect using a 2D assumption). Results from the 3D simulation clearly demonstrate a trend towards increasingly negative T-stress as one moves towards the free surface. This demonstrates the area over which plane stress conditions dominate the solution. As shown previously the reduction in T-stress as one approaches the outer surface greatly affects the through thickness average (Figure 19).

Under high in-plane constraint conditions (Figure 20b) the average T-stress through thickness is similar for all thicknesses excepting the $B = 40$ mm condition. The slight variation in average T-stress for the $B = 40$ mm condition is probably a result of the significant scatter seen for this sample, as the free surface is approached. For low constraint conditions the average T-stresses shown in Figure 20a are somewhat more pronounced in terms of each specific thickness than that noted for high in-plane constraint condi-

tions. This change in average T-stress for specific thicknesses when comparing high and low constraint conditions lends credence to the interdependency of in-plane and out-of-plane constraint [41, 10, 42].

Wallin [10] derived Equations 26 and 27 from test data to demonstrate the relationship between high constraint geometries, T-stress and low constraint estimations. In Equation 26 $T_{0_{deep}}$ represents the high constraint T_0 estimated from test data and T_0 represents a low constraint T_0 estimate. In Equation 27 K_{JcLC} represents low constraint toughness and K_{JcHC} high constraint toughness. In both Equations 26 and 27 T-stress represents the low constraint T-stress predictions calculated using FEM.

$$T_0 \approx T_{0_{deep}} + \frac{\text{T-stress}}{10 \text{ MPa}/^\circ\text{C}} \quad \text{for T-stress} < 0 \quad (26)$$

$$K_{JcLC} \approx 20 + (K_{JcHC} - 20) \exp \left(0.019 \left[\frac{-\text{T-stress}}{10} \right] \right) \quad \text{for T-stress} < 0 \quad (27)$$

Previously (see Section 3.3.4) it is shown that $T_0 = -115^\circ\text{C}$ provided the best fit to data tested in this work. The median toughness corresponding to this value of T_0 was calculated to be $193.69 \text{ MPa}\sqrt{\text{m}}$ for specimens tested at -70°C . Combining these values of T_0 and median toughness with low constraint estimates of T-stress (see Table 21) and applying Equations 26 and 27, T_0 and toughness were estimated for low constraint geometries, results are shown in Table 22. It can be seen that T_0 does not vary significantly, remaining within -5°C of the experimentally measured T_0 , for each out-of-plane constraint condition investigated. This is as expected given that predicted measures of T-stress, derived from 3D simulations, do not appear to be sig-

nificantly impacted by out-of-plane constraint. The T-stress predicted using 2D simulation differs from the experimental T_0 by ≈ -10 °C. The T-stresses predicted using 2D and 3D FEM provide estimated values of T_0 that fall within the experimentally expected standard deviation (see Table 16). Similarly the estimated low in-plane constraint toughness is conservative compared to that measured experimentally $327 \leq K_{Jc_{med}} \leq 477$ MPa \sqrt{m} . Hence Equations 26 and 27 can be used to provide conservative estimates of T_0 and $K_{Jc_{med}}$ for low in-plane constraint conditions when only high in-plane constraint data is available.

Table 22: Low constraint geometry estimates of T_0 and K_{Jc} from T-stress

B	T-stress	Estimated T_0	Estimated $K_{Jc_{med}}$
mm	MPa	°C	MPa\sqrt{m}
10	-45.50	-119.26	209.37
20	-51.08	-119.82	211.39
30	-53.84	-120.09	212.40
40	-55.52	-120.26	213.01
PE	-110.00	-125.71	234.06

4. Conclusions

1. In-plane and out-of-plane constraint conditions affect the toughness of low strength ferritic steel both in the ductile to brittle transition region and on the upper shelf. This confirms the importance of maintaining the effect of thickness in the low temperature requirements in pressure

vessel standards (e.g. PD 5500 Annex D and EN 13445 Annex B) where biaxial loading conditions can give rise to combinations of in-plane and out-of-plane effects.

2. Deeply notched ($a/W \geq 0.5$) bend tests clearly demonstrate out-of-plane (thickness) effects. This is supported by experimental fracture surface images and through thickness finite element calculations of T-stress.
3. Reducing in-plane constraint through shallow notches ($a/W = 0.2$) has a strong effect on the fracture toughness for both cleavage and ductile failures (i.e. on both the transition region and on the upper shelf). The loss of in-plane constraint for these geometries is clearly demonstrated in T-stress calculations. The use of shallow notch geometries for toughness measurements for pressurised components where biaxial loading may influence the constraint conditions must be handled with caution as out-of-plane constraint may not be modelled using these geometries.
4. The master curve approach was used to predict theoretical shifts in T_0 for this test programme which conservatively confirmed the observations of out-of-plane (thickness) effects in the fracture toughness tests.
5. There is a complex relationship between brittle and ductile interactions particularly in the upper region of the ductile to brittle transition. When ductile tearing occurs the variation in crack tip constraint influences the extent of ductile tearing, and the onset of cleavage fracture to varying degrees.
6. Theoretical estimations of stress-strain relationship for low test tem-

peratures based on room temperature data are provided in BS 7910. These estimations, which are based on quench and tempered steels, adequately predicted the yield and ultimate tensile strength behaviour of low strength ferritic steels for the temperature range tested. The elongation characteristics were not well captured however. Variation between the measured and estimated values was found to increase as test temperature reduced. The accuracy of the prediction beyond a test temperature of -70°C therefore requires further investigation.

Acknowledgements

The authors gratefully acknowledge that this work was funded by the Lloyd's Register Foundation, Grant number G_100257. We additionally thank the two anonymous reviewers for their contributions in improving the clarity of this manuscript.

References

- [1] Hadley, Isabel and Horn, Anthony, Treatment of constraint in BS 7910:2013, ISO 27306 and DNVGL-RP-F108, International Journal of Pressure Vessels and Piping 169 (2019) 77–93. doi:<https://doi.org/10.1016/j.ijpvp.2018.11.015>.
- [2] I. Hadley, S. Garwood, Prevention of brittle fracture in pressure vessels: A review of the design rules of EN 13445 Annex B and BSI PD 5500 Appendix D, International Journal of Pressure Vessels and Piping 169 (2019) 1–15. doi:<https://doi.org/10.1016/j.ijpvp.2018.11.010>.

- [3] A. N. O'Connor, C. M. Davies, S. J. Garwood, I. Hadley, Optimising the safe design of pressurised components, 2019. URL: <https://doi.org/10.1115/PVP2019-93154>. doi:[10.1115/pvp2019-93154](https://doi.org/10.1115/pvp2019-93154).
- [4] E. Hutchison, J. Wintle, A. O'Connor, E. Buennagel, C. Buhr, Fatigue reassessment to modern standards for life extension of offshore pressure vessels, 2015. doi:[10.1115/PVP2015-45485](https://doi.org/10.1115/PVP2015-45485), 10.1115/PVP2015-45485.
- [5] British Standards Institute, PD 5500:2018+A1:2018: Specification for unfired fusion welded pressure vessels, 2018.
- [6] C. S. Wiesner, S. J. Garwood, R. Sandström, D. M. Street, K. J. Coulson, Background to requirements for the prevention of brittle fracture in the European standards for unfired pressure vessels (prEN 13445) and metallic industrial piping (prEN 13480), International Journal of Pressure Vessels and Piping 78 (2001) 391–399. doi:[https://doi.org/10.1016/S0308-0161\(01\)00054-0](https://doi.org/10.1016/S0308-0161(01)00054-0).
- [7] M. Dawes, R. Denys, BS5500 Appendix D: An Assessment Based on Wide Plate Brittle Fracture Test Data, International Journal of Pressure Vessels and Piping 15 (1983) 161–192.
- [8] British Standards Institute, BS EN 13445-2:2014 + A3:2018: Unfired pressure vessels, 2018.
- [9] K. Wallin, The size effect in K_{IC} results, Engineering Fracture Mechanics 22 (1985) 149–163. doi:[https://doi.org/10.1016/0013-7944\(85\)90167-5](https://doi.org/10.1016/0013-7944(85)90167-5).

- [10] K. Wallin, Quantifying Tstress controlled constraint by the master curve transition temperature T_0 , Engineering Fracture Mechanics 68 (2001) 303–328. doi:[https://doi.org/10.1016/S0013-7944\(00\)00067-9](https://doi.org/10.1016/S0013-7944(00)00067-9).
- [11] Z. Liu, X. Wang, J. Tang, C. Deng, H. Zhao, X. Chen, The effects of in-plane and out-of-plane constraints on j-r curves for x80 steel: A study using clamped sent specimens, Engineering Fracture Mechanics 206 (2019) 342–358. doi:<https://doi.org/10.1016/j.engfracmech.2018.12.004>.
- [12] Kouzoumis, Konstantinos and Hadley, Isabel and Mostafavi, Mahmoud, Effect of Biaxiality on Engineering Critical Assessments, Procedia Structural Integrity 17 (2019) 347–354. doi:<https://doi.org/10.1016/j.prostr.2019.08.046>.
- [13] M. A. Verstraete, S. Hertelé, R. M. Denys, K. Van Minnebruggen, W. De Waele, Evaluation and interpretation of ductile crack extension in sent specimens using unloading compliance technique, Engineering Fracture Mechanics 115 (2014) 190–203. doi:<https://doi.org/10.1016/j.engfracmech.2013.11.004>.
- [14] H. Zhou, F. Biglari, C. M. Davies, A. Mehmanparast, K. M. Nikbin, Evaluation of fracture mechanics parameters for a range of weldment geometries with different mismatch ratios, Engineering Fracture Mechanics 124–125 (2014) 30–51. doi:<http://dx.doi.org/10.1016/j.engfracmech.2014.03.006>.

- [15] S. Kamel, The effects of constraint and residual Stress on ductile and brittle fracture, Thesis, Imperial College London, 2010.
- [16] IAEA, Deterministic evaluation for the integrity of reactor pressure vessel., Report, International Atomic Energy Agency IAEA, 2010.
URL: http://www-pub.iaea.org/MTCD/publications/PDF/te_1627_web.pdf.
- [17] Lidbury, D. P. G. and Sherry, A. H. and Bass, B. R. and Gilles, P. and Connors, D. and Eisele, U. and Kiem, E. and Keinanen, H. and Wallin, K. and Lauerova, D. and Marie, S. and Nagel, G. and Nilsson, K. and Siegele, D. and Wadier, Y., Validation of constraint-based methodology in structural integrity of ferritic steels for nuclear reactor pressure vessels, *Fatigue & Fracture of Engineering Materials & Structures* 29 (2006) 829–849. doi:[10.1111/j.1460-2695.2006.01057.x](https://doi.org/10.1111/j.1460-2695.2006.01057.x).
- [18] Taylor, N.G. and Bass, B. R. and Swan, D.I. and Siegele, D., NESC-IV Project: An investigation of the transferability of master curve technology to shallow flaws in reactor pressure vessel applications, Report NESCDOC-05-007, 2005.
- [19] T. D. Swankie, The role of shear and constraint in mixed mode fracture, Thesis, 1999.
- [20] Garwood, S. J., Effect of Specimen Geometry on Crack Growth Resistance Fracture Mechanics: Proceedings of the Eleventh National Symposium on Fracture Mechanics: Part I, ASTM International, West

- Conshohocken, PA, 1979. URL: https://compass.astm.org/DIGITAL_LIBRARY/STP/PAGES/STP34933S.htm. doi:978-0-8031-4746-1.
- [21] B. S. Institute, Bs en iso 3785:2006 metallic materials. designation of test specimen axes in relation to product texture, 2006.
 - [22] X.-K. Zhu, J. A. Joyce, Review of fracture toughness (g, k, j, ctod, ctoa) testing and standardization, Engineering Fracture Mechanics 85 (2012) 1–46. doi:<http://dx.doi.org/10.1016/j.engfracmech.2012.02.001>.
 - [23] ASTM, E1921-19b: Standard Test Method for Determination of Reference Temperature, To, for Ferritic Steels in the Transition Range, 2019.
 - [24] British Standards Institute, BS EN 10002-1:2001: Metallic materials - Tensile testing - Part 1: Method of test at ambient temperature, 2001.
 - [25] British Standards Institute, BS 7910:2019 Guide to methods for assessing the acceptability of flaws in metallic structures, 2019.
 - [26] ASTM, ASTM E1820-20: Standard Test Method for Measurement of Fracture Toughness, 2020. doi:<https://doi.org/10.1520/E1820-20>.
 - [27] ISO, ISO 12135:2016 Metallic materials - Unified method of test for the determination of quasistatic fracture toughness, 2016.
 - [28] Dassault Systèmes, Abaqus/cae 2018, 2017.
 - [29] Palmer, Iain and Mokhtarishirazabad, Mehdi and Moffat, Andrew and Mostafavi, Mahmoud, Effects of In-Plane and Out-of-Plane Constraint

- on Fracture Toughness in Austenitic Stainless Steel, in: ASME 2019 Pressure Vessels & Piping Conference, volume Volume 6A: Materials and Fabrication, V06AT06A012, 2019. doi:[10.1115/pvp2019-93660](https://doi.org/10.1115/pvp2019-93660).
- [30] R. S. Kulka, A. H. Sherry, Fracture toughness evaluation in c(t) specimens with reduced out-of-plane constraint, 2012. doi:[10.1115/pvp2012-78751](https://doi.org/10.1115/pvp2012-78751).
- [31] T. Anderson, Fracture mechanics: fundamentals and applications, 4 ed., Boca Raton, FL: Taylor & Francis, 2017.
- [32] A. L. V. da Costa e Silva, The effects of non-metallic inclusions on properties relevant to the performance of steel in structural and mechanical applications, Journal of Materials Research and Technology 8 (2019) 2408–2422. doi:[10.1016/j.jmrt.2019.01.009](https://doi.org/10.1016/j.jmrt.2019.01.009).
- [33] K. Törrönen, T. Saario, K. Wallin, J. Forstén, Mechanism based evaluation of materials behavior and reference curves, Nuclear Engineering and Design 81 (2019) 35–50. doi:[10.1016/0029-5493\(84\)90249-8](https://doi.org/10.1016/0029-5493(84)90249-8).
- [34] L. Xia, C. F. Shih, Ductile crack growth—III. Transition to cleavage fracture incorporating statistics, Journal of the Mechanics and Physics of Solids 44 (2006) 603–639. doi:[10.1016/0022-5096\(95\)00086-0](https://doi.org/10.1016/0022-5096(95)00086-0).
- [35] B. Tanguy, J. Besson, R. Piques, A. Pineau, Ductile to brittle transition of an A508 steel characterized by Charpy impact test: Part I: Experimental results, Engineering Fracture Mechanics 72 (2004) 49–72. doi:[10.1016/j.engfracmech.2004.03.010](https://doi.org/10.1016/j.engfracmech.2004.03.010).

- [36] A. Pineau, A. A. Benzerga, T. Pardoen, Failure of metals i: Brittle and ductile fracture, *Acta Materialia* 107 (2016) 424–483. URL: <http://www.sciencedirect.com/science/article/pii/S1359645415301403>. doi:<https://doi.org/10.1016/j.actamat.2015.12.034>.
- [37] F. Pedregosa, G. Varoquaux, A. Gramfort, V. Michel, B. Thirion, O. Grisel, M. Blondel, P. Prettenhofer, R. Weiss, V. Dubourg, J. Vanderplas, A. Passos, D. Cournapeau, M. Brucher, M. Perrot, d. Duchesnay, Scikit-learn: Machine Learning in Python, *Journal of Machine Learning Research* 12 (2011) 2825–2830. URL: <http://jmlr.org/papers/v12/pedregosa11a.html>.
- [38] M. Gupta, R. C. Alderliesten, R. Benedictus, A review of t-stress and its effects in fracture mechanics, *Engineering Fracture Mechanics* 134 (2015) 218–241. doi:<http://dx.doi.org/10.1016/j.engfracmech.2014.10.013>.
- [39] M. Mostafavi, D. J. Smith, M. J. Pavier, Reduction of measured toughness due to out-of-plane constraint in ductile fracture of aluminium alloy specimens, *Fatigue & Fracture of Engineering Materials & Structures* 33 (2010) 724–739. URL: <https://doi.org/10.1111/j.1460-2695.2010.01483.x>. doi:[10.1111/j.1460-2695.2010.01483.x](https://doi.org/10.1111/j.1460-2695.2010.01483.x).
- [40] A. H. Sherry, C. C. France, M. R. Goldthorpe, Compendium of t-stress solutions for two and three dimensional cracked geometries, *Fatigue & Fracture of Engineering Materials & Structures* 18 (1995) 141–155. doi:[10.1111/j.1460-2695.1995.tb00148.x](https://doi.org/10.1111/j.1460-2695.1995.tb00148.x).

- [41] S. M. Tonge, C. A. Simpson, C. Reinhard, T. Connolley, A. H. Sherry, T. J. Marrow, M. Mostafavi, Unifying the effects of in and out-of-plane constraint on the fracture of ductile materials, *Journal of the Mechanics and Physics of Solids* 141 (2020) 103956. doi:<https://doi.org/10.1016/j.jmps.2020.103956>.
- [42] Smith, J. A. and Rolfe, S. T., The Effect of Crack Depth (a) and Crack Depth to Width Ratio (a/W) on the Fracture Toughness of A533-B Steel, *Journal of Pressure Vessel Technology* 116 (1994) 115–121. doi:[10.1115/1.2929564](https://doi.org/10.1115/1.2929564), 10.1115/1.2929564.